Materialia 8 (2019) 100456

Contents lists available at ScienceDirect

Materialia

journal homepage: www.elsevier.com/locate/mtla

Full Length Article

Microstructure – Property correlations for additively manufactured NiTi based shape memory alloys

Sujith Kumar S[a], Lakhindra Marandi[a], Vamsi K. Balla[b,1], Sandip Bysakh[b], David Piorunek[c], Gunther Eggeler[c], Mitun Das[b,2], Indrani Sen[a,*]

[a] Department of Metallurgical and Materials Engineering, Indian Institute of Technology Kharagpur, India
[b] Bioceramics and Coating Division, CSIR – Central Glass and Ceramic Research Institute, Kolkata, India
[c] Institute for Materials, Ruhr-University Bochum, Bochum, Germany

ARTICLE INFO

Keywords:
NiTi based shape memory alloys
Pseudoelasticity
Additive manufacturing
LENS
Microstructure
Spherical nanoindentation

ABSTRACT

The research focuses on systematically studying the effect of processing parameters in controlling the microstructure and mechanical behavior including pseudoelasticity of a NiTi alloy. The alloy is prepared by laser engineered net shaping (*LENS*) based additive manufacturing technique. Laser energy densities of the manufacturing method are modified by altering laser scan speed and power. Corresponding effects on microstructure and phase evolution of NiTi alloy are evaluated thoroughly. Subsequently, mechanical properties are assessed implementing macro-, micro- and nano-indentations with load levels varying over five orders of magnitude. Layered microstructures, as a signature of the manufacturing process, are evident from the front and side planes of the products. Interestingly, existence of trace volume fraction of precipitates and martensite phase are noted in the alloy manufactured with highest laser energy density. These influence hardness, elastic modulus and indentation size effect of the alloy. Most importantly, pseudoelastic recovery of NiTi gets adversely affected. Spherical-nanoindentation is performed to precisely assess pseudoelasticity of NiTi alloys. Indentation-stress–strain graphs are generated from the spherical-nanoindentation. This is a unique and state-of-the-art way to assess the localized mechanical performance of materials. Considering that additive manufacturing is associated with microstructural inhomogeneity thereby leading to property variation along different regions, investigation is corroborated with bulk-scale tensile testing of the alloys, revealing similar results. Subsequent cyclic tensile tests complemented with digital image correlation are performed to appreciate their strain-recoverabilities. This study provides a scope to optimize the parameters of *LENS* to manufacture NiTi with the best combination of microstructure, phase stability and pseudoelasticity.

1. Introduction

NiTi, popularly known as Nitinol, is the most widely used shape memory alloys (SMAs) having unique and smart functional characteristics such as shape memory effect (*SME*) and pseudoelastic effect (*PE*). Owing to these attractive properties, NiTi has found usage in a wide variety of applications and gained immense interests from the scientific and engineering communities. By virtue of the *SME*, NiTi undergoes a reversible and recoverable phase transformation from the parent austenite phase with cubic (*B2*) structure to a monoclinic (*B19′*) martensite phase. This happens primarily with the change in temperature and stress level. These materials in the *PE* state, upon loading, undergo stress-induced martensitic transformation (*SIMT*) from the parent austenite phase. During unloading, the martensite phase reverts back to the parent austenite phase. Consequently, the reversible phase transformation in this alloy generates a recoverable strain of ~8–10% [1–5]. Owing to the high level of strain recoverability of this alloy associated with the unique *SME* and *PE* behavior, along with a combination of higher specific strength, better corrosion resistance and biocompatibility, *SMAs* are increasingly deployed in a wide variety of technologies. For instance, NiTi alloys are especially used in smart devices, *MEMS* and actuators, as well as in various biomedical applications such as stents and guide wires [1–3,5–8]. In many cases, such applications however demand for complex component shapes and apply multi-axial small scale loads.

With the recent advancement of technologies, latest manufacturing methods are upgraded to such a level that near net shape components

* Corresponding author.
E-mail address: indrani.sen@metal.iitkgp.ac.in (I. Sen).
[1] Currently at Materials Innovation Guild, Department of Mechanical Engineering, University of Louisville, Louisville, KY 40208, United States.
[2] Currently at Department of Materials Science and Engineering, Faculty of Engineering, Tel-Aviv University, Israel.

https://doi.org/10.1016/j.mtla.2019.100456
Received 5 April 2019; Accepted 23 August 2019
Available online 27 August 2019

can be directly produced in a single step. This certainly eliminates the intermediate production routes. Consequently, the processing complexities reduce which in turn cuts down the production cost as well as time. Moreover, even complex shaped components with high dimensional accuracies and precisions are produced. Additive manufacturing (*AM*) is one such technique for manufacturing near net shape products. In this method, a prototype of final product is designed in computer aided design (*CAD*). Based on the design, the entire product is sliced into various sections. Subsequently, the final product or component is manufactured with layer by layer deposition or printing as per the *CAD* [9]. Consequently, *AM* can produce the required shape with high accuracy. Nevertheless, the complications in the manufacturing methods lead to completely different microstructural evolution in the product in comparison to that of the conventional one. Such variations in the microstructure can in many ways affect their properties. Hence, any such processing based microstructural modifications needs to be well studied a priori. Furthermore, even the variation in *AM* processing parameters is noted to alter the properties of the manufactured components. Hence, optimized processing conditions are solicited to achieve the desired product [10–12].

Amongst the different types of additive manufacturing processes, Laser Engineered Net Shaping (*LENS*) is a well-known and widely used one [13–18]. As per this processing method, a high energy laser beam is used for melting the pre-alloyed powder on a substrate. This is followed by its rapid solidification. Raster movement of the laser, as controlled by the *CAD* generates the shape of the final product. It is noteworthy that producing NiTi based components using *LENS* technique is promising in many ways in comparison to that achieved by conventional metallurgical methods. This includes achieving better surface finish accuracies and desired levels of porosity in the processed component, as observed for the Co based alloys processed through *LENS* [19]. Furthermore, the microstructural size and morphologies and consequently the aimed properties of the end product can be tailored by altering the various processing parameters of *LENS*. For instance, decrease in laser power as well as increase in its scan speed leads to formation of porous materials, which are in demand for biomedical implants [19]. Similar microstructure development as well as porosity generation is therefore expected for NiTi components manufactured by the *LENS* method, as well. Nevertheless, it is important to perform a systematic study on how the microstructure evolves and affects the corresponding properties in the *LENS* manufactured NiTi, at the first place.

It is noteworthy that retaining mechanical and shape memory properties of NiTi while fabricating complex shapes in a single step is still a foremost challenge. This is particularly because of the sensitiveness of NiTi on the factors such as its exact atomic composition, grain size and phase fraction. It is noteworthy that even nominal alterations in these factors during fabrication may change the thermal transformation characteristics, elastic moduli, and overall recoverable strain of the NiTi alloy [13,20–22]. The *LENS* process on the other hand, leaves traces of microstructural and morphological signatures of the layer by layer deposition process in the finished component, which is relevant for NiTi as well [9,13,23]. This is expected to modify all the associated properties of the alloy as well. To appreciate the role of *LENS* parameters for successfully producing NiTi with the desired characteristics, it is important to develop a thorough understanding of the processing – microstructure – property relations for the alloy and the manufacturing method.

A few previous attempts were made to study the role of varying process parameters in controlling the properties of the *LENS* processed NiTi alloy which requires further in-depth investigation [13–15]. In this research, a systematic study has been performed to assess the influence of *LENS* processing parameters such as laser power, scan speed or energy density in affecting the microstructure, crystallography as well as phase evolution in the alloy. The investigation further focuses on correlating these microstructural modifications with the global and local mechanical properties including the unique pseudoelastic characteristics of the NiTi alloy. Detailed microstructural investigation involving optical, scanning and transmission electron microscopies, X-ray analysis and calorimetry are performed to meet the first objective. Furthermore, variation in hardness and the modulus of the alloy at different length scales as well as the effects of processing conditions on them are thoroughly characterized by implementing macro as well as instrumented micro- and nano- indentation techniques. Considering the importance of application of load levels at small scale in the NiTi based components, indentation size effect of the *LENS* processed NiTi alloy is extensively studied as well. Alteration in the processing parameters is noted to control the microstructure and phase evolution in NiTi alloy. However, it is noteworthy that such modifications are not reflected in significantly modifying their conventional mechanical properties such as hardness or elastic modulus. Pseudoelastic characteristics of the alloy, on the other hand, get considerably affected on changing the processing parameters of *LENS*. This is particularly appreciated by implementing nanoindentation with sphero-conical indenter tips. Additionally, indentation stress–strain curves are generated from the nanoindentation results to appreciate the localized mechanical properties of the pseudoelastic NiTi alloy further. It is noteworthy that small scale conventional mechanical testing of materials is difficult and expensive to perform. Rather similar information can be extracted from the indentation stress–strain curves. Such curves are uniquely generated for the first time for the NiTi based pseudoelastic alloy in this study.

2. Materials and experiments

2.1. Sample preparation

NiTi powder having chemical composition of 50.04% Ni, 0.002% N, 0.006% C and 0.22% O, the rest being Ti (at.%) is used in the current study to additively manufacture bulk NiTi products. The gas atomized spherical solid powders with particle size varying in the range of 50–150 μm was supplied by *ATI Powder Metals, PA, USA* [24]. Hardly any presence of satellites was noted in the powder. NiTi specimens were fabricated using the *LENS*^{TM} system (*MR7, Optomec Inc. Albuquerque, NM*). The entire fabrication process was carried out inside a glove box in argon atmosphere. Moreover, oxygen content of the system was maintained to a level of <10 ppm. The Ar atmosphere as well as low oxygen level ensured avoidance of oxidation to NiTi alloy during the manufacturing stage. This is primarily important considering the fact that a minor change in the alloy composition leads to significant alteration in the *SMA*s transformation characteristics as well as the mechanical performance [20,22,24,25]. Initially, a molten metal pool generated, on focusing the laser beam upon a 3 mm thick CP-Ti metal substrate. Subsequently, NiTi powder from the feed stock was injected and rastered back and forth onto the molten metal pool. The powder instantly melted and spread uniformly over the substrate. This was followed by almost simultaneous solidification of the molten NiTi into a finite thickness. The solidification was thereby associated with a very high cooling rate. Based on the *CAD* model, the process was repeated in alternate perpendicular directions. This resulted to a gain in the vertical dimension. The desired shape was thereby achieved according to the layer-by-layer deposition process. For the present study, cuboid NiTi specimens of dimension 60 mm × 12 mm × 2.8 mm were prepared by the *LENS* method. The different parameters for this laser based process such as laser scan speed (v) and power (P) are varied to achieve different laser energy densities (E) as per the following relation [23,26]:

$$E = \frac{P}{v \times d} \tag{1}$$

Constant beam diameter ($d = 0.5$ mm) was maintained for all the experiments. The process parameters such as v and P however were varied, as mentioned in Table 1, to obtain three different laser energy densities. The subsequent products manufactured with increasing laser energy densities are named as $NiTi_{\_E1}$, $NiTi_{\_E2}$, and $NiTi_{\_E3}$, respectively. Consequently, variations in the microstructure, phase evolution as well

Table 1
Variation in the *LENS* processing parameters for manufacturing bulk NiTi alloys.

Alloy	Laser power (w)	Scan speed (mm/s)	Laser energy (J/mm^2)
NiTi$_{_E1}$	200	15	27
NiTi$_{_E2}$	300	15	40
NiTi$_{_E3}$	350	10	70

as mechanical properties of the finished products are expected which are being characterized and investigated next.

2.2. Microstructure analysis

After fabrication, as a first step, microstructures of all the specimens both along the surface as well as across the horizontal and vertical cross-sections were thoroughly investigated. Detailed microstructural characterization of the NiTi$_{_E1}$, NiTi$_{_E2}$, and NiTi$_{_E3}$ specimens were performed using both optical microscope (*Zeiss Axiovert; Leica DM 2700 M*) as well as scanning electron microscope (*Zeiss EVO 60*). The specimens were initially cut into rectangular pieces of dimensions 10 mm × 4 mm × 3 mm and sequentially polished using the standard metallographic techniques. The final polishing was carried out using diamond paste of size 1 μm as well as colloidal silica solution. These fine polishing steps ensured proper surface finish of the specimens by removing any polishing induced transformed martensite. The polished specimens were next etched using a water-based reagent comprising of HNO_3 and *HF* for 1 min. Colored optical images were further obtained using tint etchant comprising primarily of hydrochloric acid, Ammonium hydrogen fluoride and potassium disulphate.

Electron back scatter diffraction (*EBSD*) was performed next for the *LENS* manufactured NiTi alloys (using *Zeiss Auriga compact*). For this, the initially well-polished specimens were electro-polished apriori using *Struers, LectroPol-5*. An electrolyte, consisting of Acetic acid and perchloric acid was used for the purpose. A voltage of 10 V was applied for 20 s to secure best surface finish. The surface quality was reciprocated in obtaining more than 95% indexing in the *EBSD* analysis. A voltage of 25 kV and step size of 3 μm were used for the *EBSD* analysis.

To analyze the microstructural details of the *LENS* manufactured alloys further, transmission electron microscopy (*TEM*) of the specimens were performed. *TEM* specimens were extracted from the as deposited samples using low speed precision diamond saw (*Buehler Inc., USA*). The cut specimens were next ground and polished to achieve a thickness of 0.1 mm. Further, circular disks were cut and dimpled using Gatan dimple grinder until a thickness of 40 μm at its center is obtained. These dimpled samples were then Argon ion-milled in a Precision Ion Polishing System (*PIPS*) to achieve electron transparency. A high-resolution *TEM* (*Tecnai G^2 30ST,* FEI Company, USA) operating at 300 kV was used to characterize the microstructure to greater details. Selected area diffraction was used for phase identification and crystal orientation determination. The microscope is equipped with a 1k by 1k Multi-Scan *CCD* Camera for digital imaging and an energy dispersive X-ray spectroscopy (*EDS*) system (*EDAX Inc., USA*) to perform local chemical analysis.

Porosity generated in the *LENS* processed alloy was next characterized using the X-ray micro computed tomography technique (*GE pheonix vtomex*). A combination of voltage and current of 110 kV and 100 μA respectively was used to capture the images. 1000 frames were captured at a rate of 500 ms per image. Voxel resolution to capture each image is maintained to 11 μm.

2.3. Phase and thermal analysis

Crystallographic phases of the NiTi alloy were analyzed using the X-ray diffractometer (*X'Pert ProMPD, PANalytical, USA*). The diffractometer used Cu–Kα radiation, operating at a combination of voltage and current of 40 kV and 40 mA, respectively. The 2θ angle was varied from 20° to 100° and a scan rate of 2° per minute was maintained. PANalytical- X'Pert High Score software was used to analyze the *XRD* results. Different phases were noted to be present in the NiTi$_{_E1}$, NiTi$_{_E2}$, and NiTi$_{_E3}$ specimens as discussed in the next section.

Transformation temperatures of all the NiTi based shape memory alloy were characterized subsequently using a Differential Scanning Calorimeter, *DSC* (*Netzsch DSC 204 F1*). Small sized specimens weighing around 50 mg were used for this. Specimens were carefully cut using slow cutting rate across the mid-section, to avoid the surface oxide layer, if any. Moreover, the cut specimens were subsequently ground and polished to achieve flat surfaces. Experiments were conducted over the temperature range of ±150 °C with a heating/cooling rate of 10 °C/min [27]. Starting from the room temperature, the test temperatures were varied in cycles to generate the thermograms for heat flow vs. temperatures for all the *LENS* manufactured NiTi aloys. The characteristic peaks on such *DSC* thermograms represent the phase transformation of the NiTi alloy.

2.4. Mechanical testing

Further to the microstructural and crystallographic investigations, indentations at different load levels were performed. Samples for indentation tests were metallographically ground and polished and the final stage of polishing was performed using a colloidal silica suspension. This ensured smoothest surface finish devoid of polishing induced martensite, which are important for precise indentation experimentations. Initially, hardness of all the NiTi$_{_E1}$, NiTi$_{_E2}$, and NiTi$_{_E3}$ alloys at macro-scale was determined using macro-Vickers indenter (*Leco Vickers Hardness Tester, LV 700*). A maximum load of 500 N and a dwell time of 10 s was used for the experiments. Furthermore, to assess the occurrence of size effect, if any, macro-indentations were also performed with decreasing load levels of 300 N, 200 N, 100 N and 50 N.

In a similar way, properties of the alloys such as hardness and elastic modulus at micro- and nano-scales were further analyzed using the instrumented indentation technique (*Anton Paar, Model: NHT3*). Standard geometrically self-similar Vickers and Berkovich diamond indenter tips with respective tip diameters of ~200 nm and 100 nm were used for the micro- and nano-indentations respectively. Prior to the experiments, area functions of the indenter tips were calibrated by performing indentation on standard specimens of steel and fused silica. To assure stabilizations in temperature and mechanical vibrations due to handling the specimens to the experimental setup, they were placed in the instrument for at least 2 h prior to the experiments [28,29]. Zero-point corrections were performed before analyzing the data. Initially, load-controlled micro-indentations were performed using three different load levels of 1, 3 and 5 N. At least 10 indentations were performed at each load levels. Nano-indentations at a lower load levels of 3, 5 and 7 mN were performed next. Both the micro- and nano-indentations were performed over a range of load levels to assess the size effect of the *LENS* processed NiTi alloys. In all the respective cases of macro-, micro- and nano-indentations, a minimum of 10 indentations were performed at each load levels in the individual alloy specimens. The mean values of hardness and elastic modulus for each alloy, as obtained from the experiments are reported. In all cases, the standard deviation values are also provided along with, to appreciate the scatter in the data.

Furthermore, apart from assessing the elastic and plastic deformation behavior of NiTi alloys using sharp indenter tips, nano-indentations were also performed with blunt spherical indenter of tip diameter 40 μm. A maximum load of 5 mN was used for this. The primary purpose was to appreciate the pseudoelastic characteristics of the alloys. While the load-displacement data obtained from the spherical nanoindentation experiments estimate the permanent and recoverable deformation of the alloys, indentation stress–strain curves generated therein precisely assess the elastic, pseudoelastic and plastic deformation behavior of NiTi.

Next, room temperature tensile tests of the NiTi$_{_E1}$, NiTi$_{_E2}$ and NiTi$_{_E3}$ alloys were performed using the universal testing machine

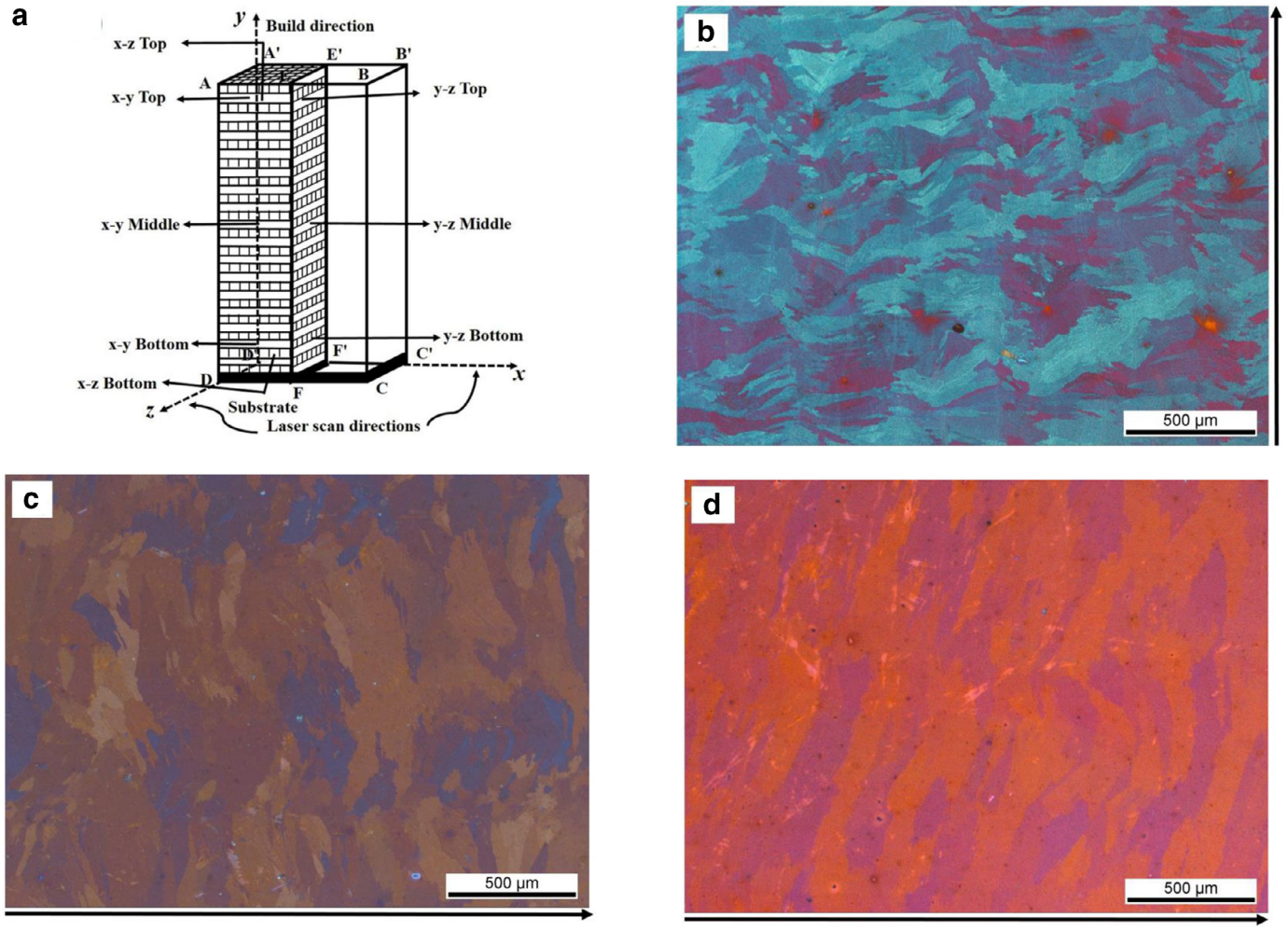

Fig. 1. (a) Schematic representation of a specimen produced by the *LENS* process. The laser scan and build directions are represented by arrows. The various planes and locations used for characterizing the microstructure of the as-build alloys along the *x–y, y–z* and *x–z* planes are marked in the figure. Representative optical micrographs of (b) $NiTi_{\_E1}$, (c) $NiTi_{\_E2}$ and (d) $NiTi_{\_E3}$ alloy specimens captured from *x–y*-middle as highlighted in Fig. 1(a). Build direction is marked with an arrow. Color contrasts in the micrographs are achieved using polarized light and differential interference contrast on the tint etched specimens. (For interpretation of the references to colour in this figure legend, the reader is referred to the web version of this article).

(*Instron 3365, USA*) as per the ASTM standard [30]. Flat dog-bone shaped specimens with the reduced section length of 16 mm as well as thickness of 1.6 mm were used for the purpose. The specimens were machined in such a way that the tensile axis and the gage length is oriented along the build direction. All the strengths and strains of the NiTi specimens manufactured by *LENS* were estimated from the tests. Tensile tests for each category of alloys were repeated and the mean values are reported.

Subsequent to the conventional way of assessing the tensile behavior of the alloys, cyclic tensile tests were performed in association of digital image correlation (*DIC*). The setup from *GOM-Aramis Education* and the associated software GOM-correlate was used for the purpose. Prior to the tests, a random speckle pattern with white background and black spots were spray painted on the surface of the polished tensile specimens. Dual cameras with 5MP resolution (spatial resolution of 2448×2050 pixels) and focal length of 12.5 mm were adjusted to capture the 3D images for the central part of the tensile specimens. Tensile tests were performed while the specimens were loaded till a strain level of 1.5%. Next, the specimens were subsequently unloaded to zero. Such a loading–unloading tensile test approach is termed as cyclic-tensile test. The cycles were repeated twice for each specimens. Extensometer of length 12.5 mm were mounted on the gage section of the specimens to precisely capture the strain generated during deformation. Complementary to this, as the tensile test progresses, images were also captured particularly, on the central part of the gage section by the *DIC* setup at a frequency of 14 Hz. Consequently, the strain distribution and progression at this part was measured throughout the test. The purpose is to appreciate the in-situ strain variation and subsequent strain recoverability of the specimens upon unloading.

3. Results and discussion

3.1. Microstructure

Schematic representation of a specimen produced by *LENS* is presented in Fig. 1(a). The build direction along with the laser scan directions for the process is evident from the schematic. Also, formation of the layered structure owing to the layer by layer deposition of the metal powder is apparent from this figure. It is noteworthy that additive manufacturing is primarily associated with layered and non-uniform microstructures which are expected to affect the mechanical properties of an alloy. To develop a detailed insight on the microstructural evolution of the NiTi alloys, systematic microstructural characterizations for the surface and cross-sections of the as-produced $NiTi_{\_E1}$, $NiTi_{\_E2}$ and $NiTi_{\_E3}$ alloys are performed. Accordingly, microstructural variations are characterized at different locations such as the bottom (near to the substrate), middle and top (near to finishing surface) zones along

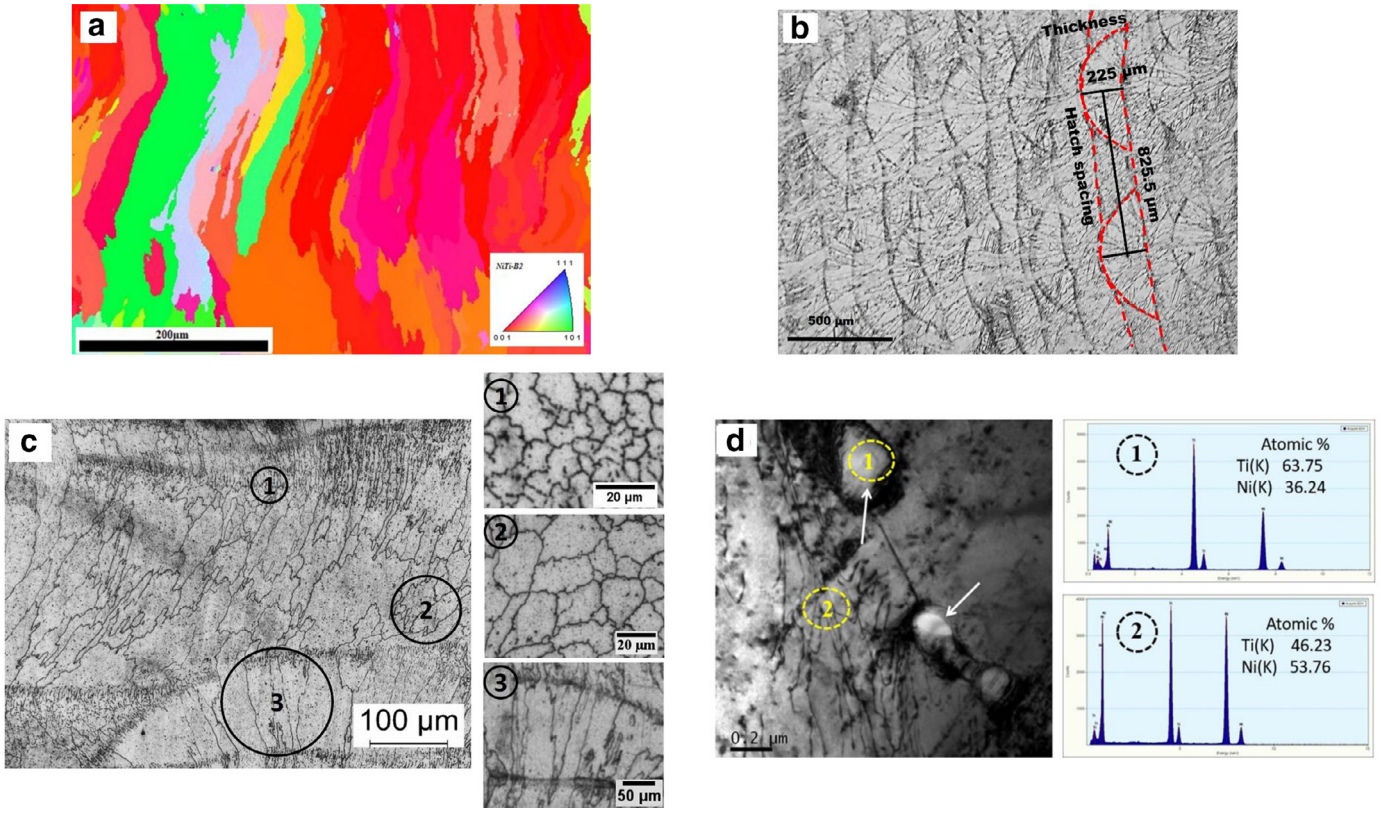

Fig. 2. (a) Representative electron back scattered inverse pole figure map of *LENS* manufactured NiTi alloy revealing signatures of layer by layer deposition process. Color codes for the different grain orientations is presented at the inset. (b) Low magnification optical micrograph of $NiTi_{\_E1}$ alloy. The hatch loops signifying the impression of laser tips and the subsequent alternate layers formed, are apparent from the micrograph. Two of the loops and consecutive layer boundaries are highlighted and the corresponding hatch spacing and layer thickness are indicated. (c) Microstructure of the $NiTi_{\_E1}$ showing different regions comprising of grains of varying size and morphology. Such different regions are marked as (1) fine equiaxed (2) coarse equiaxed and (3) columnar grains. The difference is more apparent from the higher magnification images, presented for the regions 1, 2 and 3. (d) Bright-field *TEM* image of $NiTi_{\_E3}$ specimen. Precipitates noted are pointed with arrows. *EDS* spectra collected from the precipitate and the neighboring region, marked as region 1 and 2 respectively are also provided adjacently. (For interpretation of the references to colour in this figure legend, the reader is referred to the web version of this article)

the front (*x*–*y*), side (*y*–*z*) and cross-section (*z*–*x*) planes, as marked in Fig. 1(a). However, not much effect of directions on the microstructure evolution are apparent, particularly for the front and side planes. This is also supporting the fact that the laser scan direction alters by 90° at every consecutive layer. However, while layered structures with high aspect ratio grains are observed for these two planes, equiaxed grains prevail along the cross-sectional *x*–*z* planes.

Optical microstructures with distinct color contrasts are captured using polarized lights and differential interference contrast for all the three *LENS* manufactured NiTi specimens. Representative micrographs obtained from the middle region of the *x*–*y* plane for the $NiTi_{\_E1}$, $NiTi_{\_E2}$, and $NiTi_{\_E3}$ alloys are shown in Fig. 1(b) to–(d) respectively. The build directions are marked with the arrows. Different color contrasts signify the variation in orientation at the different layers.

Non-homogeneous nature of the microstructure is distinctly apparent from the figures. The signatures of the layer by layer deposition procedure of the *LENS* based additive manufacturing method is more clearly evident from Fig. 2(a). This represents an orientation inverse pole figure map as obtained from the *EBSD* investigation of the $NiTi_{\_E1}$ alloy.

On careful scrutiny of the optical and *EBSD* micrographs for the additively manufactured NiTi alloys, signatures of the layer by layer, laser based processing become prominent. A representative optical micrograph obtained from the central part of the front plane of $NiTi_{\_E1}$ alloy is presented in Fig. 2(b). Existence of semi-circular loops, signifying the trace of the laser tip and formation of the parallel layers are evident in the microstructure. Similar features are noted for other alloys manufactured by laser based additive manufacturing process as well [31,32]. Few such loops and layer are highlighted in Fig. 2(b). As explained in the experimental section, such loops are noted to form at alternate layers since the laser direction is altered by 90° in every consecutive layers. The hatch spacing and the layer thickness signifying the distance between two such loops and the radius of the loops respectively are marked in Fig. 2(b) [31,33]. All such dimensions are estimated for the alloys. Layer thickness of the $NiTi_{\_E1}$, $NiTi_{\_E2}$ and $NiTi_{\_E3}$ alloy specimens are estimated to be ~340 ± 40 μm, 327 ± 59 μm and 258 ± 33 μm, respectively. It is therefore apparent that as the laser energy during the manufacturing increases from $NiTi_{\_E1}$ to that of $NiTi_{\_E3}$, higher heat content of the system during the subsequent processing takes a lead in compacting the layers. Hence, reduced layer thickness is observed for $NiTi_{\_E3}$. Hatch spacing on other hand, is primarily controlled by the tip size and is therefore independent of the laser energy density of the manufacturing process. The hatch spacing of the alloys is noted to be ~827 ± 31 μm.

Higher magnification micrographs on the other hand, reveals existence of varying microstructural features having different morphologies and dimension. In support of this, a representative optical micrograph captured from the middle region of the *x*–*y* plane of the $NiTi_{\_E1}$ alloy is presented in Fig. 2(c). The image reveals that the overall microstructure of the *LENS* processed NiTi comprises of three distinct zones with different grain morphologies such as fine equiaxed (*FE*), coarse equiaxed (*CE*) and columnar (*CL*) grains marked as (1), (2) and (3), respectively in Fig. 2(c). The differences in the size and morphology are clearly evident from the higher magnification images of each of these *FE, CE* and *CL* zones presented in corroboration. On quantifying the sizes of the various microstructural features (using the linear intercept method), it is noted

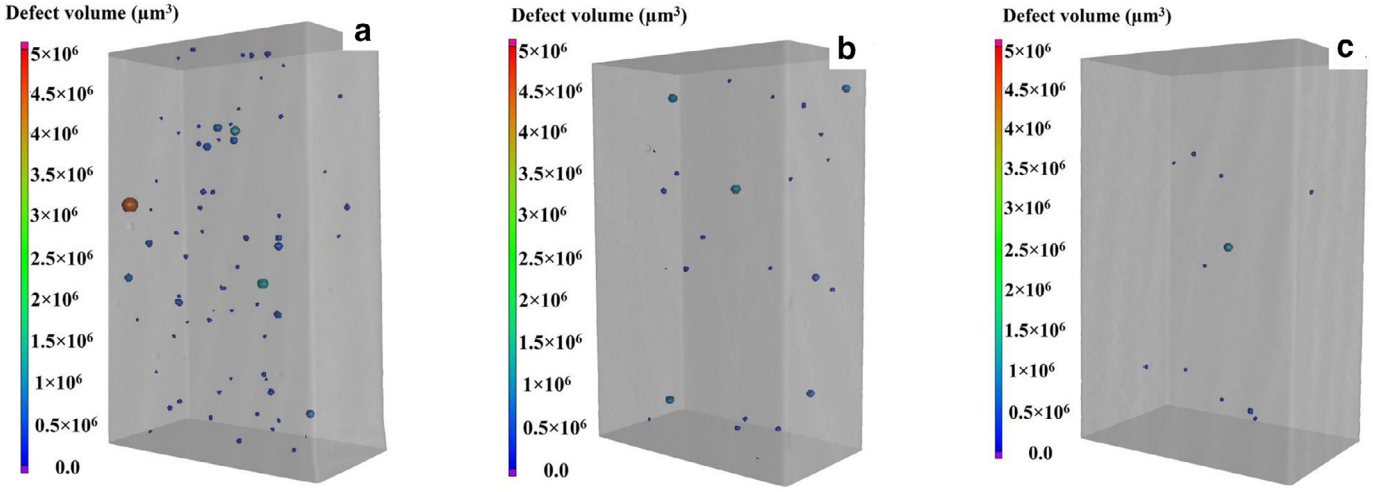

Fig. 3. Representative micro-*CT* scan images of (a) $NiTi_{\_E1}$ (b) $NiTi_{\_E2}$ (c) $NiTi_{\_E3}$ alloys manufactured by the *LENS* method. Color coded volumetric scale is provided adjacent to the figures. Reduction in the overall pore volume fraction and size to almost half its initial values is noted with increase in the laser energy densities of the manufacturing method. (For interpretation of the references to colour in this figure legend, the reader is referred to the web version of this article)

that the average size of the finer grains (16 ± 6 μm) is almost a quarter to that of the coarse grains (73 ± 9 μm). The *CL* grains on the other hand maintained an aspect ratio of ≈6 with width of ≈31 μm. It is noteworthy that grains of such different sizes and morphologies are generated owing to the unique characteristics of the *LENS* process. This includes layered deposition, multiple melting and subsequent solidification steps as well as reheating cycles as experienced by each layers. During the layer by layer deposition process, the pre-formed regions eventually get repeatedly heat treated as the subsequent layers are being formed [13,34,35]. Nevertheless, while forming a particular layer, the outer part cools at a faster rate. This leads to formation of fine equiaxed grains. In contrary, the inner part of the layer that sustains a continuous higher temperature, form coarse equiaxed grains. The junction of the laser tip, on the other hand, forms the semi-circular zone, as shown in Fig. 2(b). The combined melting of subsequent layers in this zone leads to the directional solidification and formation of columnar grains [34]. In the subsequent layers, however, only the cross sections of those columnar layers are viewed as equiaxed grains owing to the alteration in the laser rastering direction. Similar characteristics and morphologically varying features are therefore observed in all the layers. [13–16,23].

The microstructure seems to get homogenized for the $NiTi_{\_E3}$ alloy, possibly owing to the higher laser energy density and heat content during the manufacturing process. However, for this alloy, presence of precipitates of size ≈200 nm in the matrix is noticed as revealed by *TEM* investigation. A representative bright field *TEM* image for the $NiTi_{\_E3}$ specimen is presented in Fig. 2(d), where such particles are highlighted by white arrows. No such particles however are detected in the other two alloys. This indicates that the precipitates might have formed in a negligible amount in case of $NiTi_{\_E1}$ and $NiTi_{\_E2}$ alloys owing to the reduced laser energy densities. Hence, they could not be traced in the TEM study. *EDS* of the particles, marked as (1) confirmed its composition as Ti_2Ni.

It is noteworthy that previous research on laser deposited equiatomic NiTi did reveal formation of Ti_2Ni precipitates. The rapid solidification technique associated with the manufacturing method as well as the increased oxygen content in the NiTi alloy produced with higher laser energy are counted as the possible reasons for that [2,36–38]. Similar phenomena of high cooling rate is also active during the *LENS* processing and particularly for the $NiTi_{\_E3}$ alloy manufactured with the highest energy density. This alloy is expected to achieve highest peak temperature prior to its cooling to room temperature, thereby experiencing highest cooling rate. Moreover, aging treatment during the formation of subsequent layers also facilitate the precipitate formation. Furthermore, increase in oxygen absorption is also noted previously in NiTi alloy manufactured using higher energy densities for selective laser melting process [10–12]. In a similar line, possible existence of higher oxygen concentration in case of the alloy manufactured with highest laser energy i.e. $NiTi_{\_E3}$ alloy can further justify the formation of the precipitates in this alloy. *EDS* quantification confirms that the matrix adjacent to the precipitates, marked as (2) in Fig. 2(d) is Ti-lean NiTi. Such decrement in the Ti content of the matrix has also been noted in earlier studies owing to the presence of Ti-rich precipitates [39].

Apart from the apparent microstructural modification, layer by layer additive manufacturing process is viable to develop porosity in the microstructure as well. Considering that porosity plays a pivotal role in modifying the mechanical properties of NiTi, it is important to quantify the pores developed in the NiTi alloys and therefore to assess the roles played by the operating parameters of *LENS*. Representative 3-D micro-CT images for the $NiTi_{\_E1}$, $NiTi_{\_E2}$ and $NiTi_{\_E3}$ alloy specimens are presented in Fig. 3 along with the respective color coded volumetric scale bar. Varying processing parameters as well as the laser energy densities of the *LENS* process is noted to dominantly control the number and size of pores in the bulk NiTi alloy.

As a first look, it is evident from the figures that the overall pore volume fraction is more pronounced in the $NiTi_{\_E1}$ alloy. This is followed by the $NiTi_{\_E2}$ and $NiTi_{\_E3}$ alloys. Detailed quantitative analysis reveals that the alloy processed with the lowest energy, $NiTi_{\_E1}$ consists of micro pores of diameter ~76.1 ± 27 μm. With increase in the laser energy densities during the manufacturing by ~50 and ~150% for the $NiTi_{\_E2}$ and $NiTi_{\_E3}$ alloys, the pore size is however noted to decrease to 54 ± 25 μm and 37.8 ± 19.3 μm, respectively. Nevertheless, the maximum pore size is noted to decrease from 196 μm in case of $NiTi_{\_E1}$ to 101 and 67 μm for the $NiTi_{\_E2}$ and $NiTi_{\_E3}$ alloys, respectively. This signifies that as the laser energy increases by more than 2.5 fold, the pore size reduces by ~50%. It is noteworthy that higher energy input for producing $NiTi_{\_E3}$ (70 J/mm^2) is associated with better and uniform melting of the powdered metal charging. Additionally, occurrence of consistent higher temperature and therefore simultaneous heat treatment of the pre-formed layers poses possibilities to close the pores, thereby leading to reduced porosity for the $NiTi_{\_E3}$ alloy [9,10,16].

3.2. Phase analysis

Evolution of crystallographic phases in the NiTi alloy owing to the variation in processing parameters of *LENS* is thoroughly analyzed next. Room temperature *XRD* for all the $NiTi_{\_E1}$, $NiTi_{\_E2}$, and $NiTi_{\_E3}$ alloys along with the prealloyed NiTi powder are performed. Fig. 4(a) depicts the representative *XRD* plots for them.

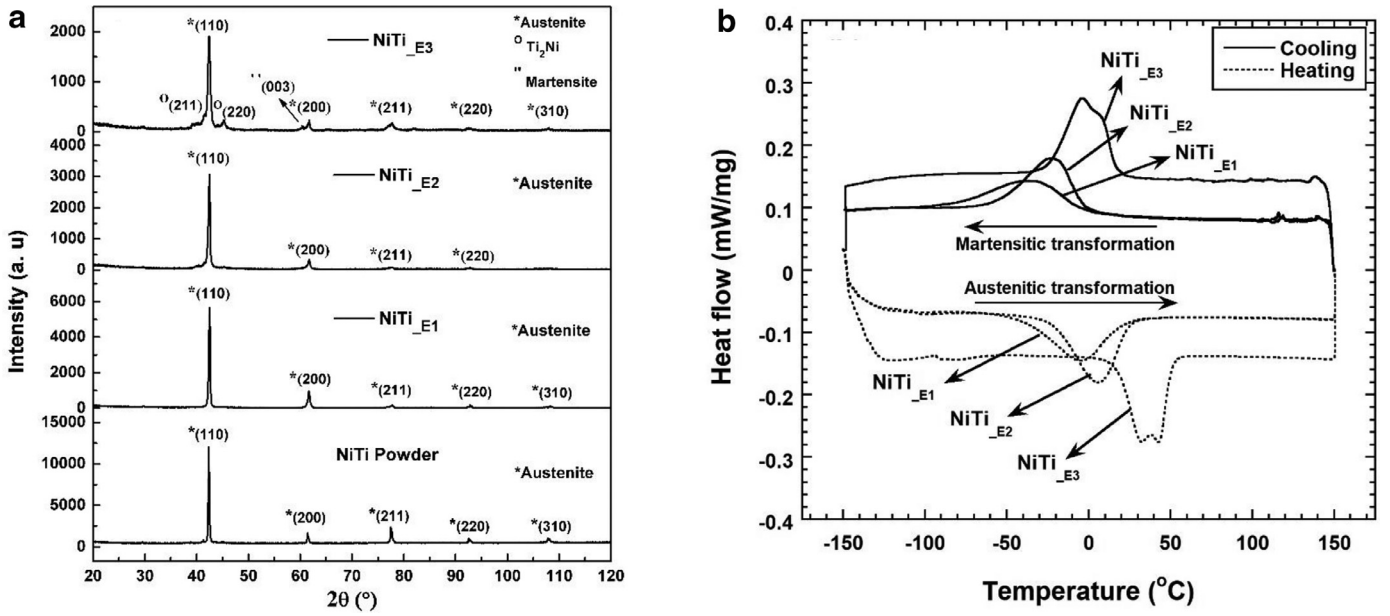

Fig. 4. (a) *X*-ray diffraction results of the as-received NiTi-powder and *LENS* manufactured $NiTi_{\_E1}$, $NiTi_{\_E2}$ and $NiTi_{\_E3}$ alloys. Occurrence of Ti_2Ni precipitates as well as a feeble peak of martensite (indicated by an arrow) in the $NiTi_{\_E3}$ alloy are evident from the plot. The powder as well as $NiTi_{\_E11}$ and $NiTi_{\_E2}$ alloys are noted to consist of B2 austenite phase. (b) Differential scanning calorimetry thermograms for $NiTi_{\_E1}$, $NiTi_{\_E2}$, and $NiTi_{\_E3}$ alloys. While complete reversible transformation is noted for the first two alloys at room temperature, $NiTi_{\_E3}$ alloy shows indication of double peaks and austenite finish at a temperature higher than ambient.

The diffraction pattern for the NiTi powder clearly shows existence of single austenitic phase which matches with the relevant 2θ peaks for the *B2* phase. It is also evident from the plots that both $NiTi_{\_E1}$ and $NiTi_{\_E2}$ specimens primarily consist of the austenite phase. However, occurrence of Ti_2Ni precipitates is evident from the *XRD* plot of $NiTi_{\_E3}$ specimen. Such existence of Ti_2Ni precipitates in case of the NiTi alloy produced with the highest laser energy density further supports the *TEM* observation. A feeble peak of martensite is also evident specifically in the $NiTi_{\_E3}$ alloy, as indicated by an arrow in Fig. 4(a). Such existence of martensite at room temperature has also been noted in the earlier investigations on NiTi [20]. Possibility of occurrence of martensite at room temperature in this alloy is further supported by the investigation of the transformation characteristics of the *LENS* manufactured alloys. This certifies that change in laser energy density plays a crucial role in controlling the phase evolution in this functional material.

3.3. Thermal analysis

The representative temperature vs. heat flow diagrams for all the laser deposited specimens are presented in Fig. 4(b).

The specimens are initially heated to +150 °C. This is to ensure complete transformation to the high temperature austenite phase. This is followed by cooling the specimen down to –150 °C. The solid lines as well as the positive peaks in the *DSC* thermogram indicate transformation of the parent austenite to martensite phase. The dotted lines, on the other hand, represent re-heating the specimen to +150 °C. The negative peaks thus obtained therefore indicate reverse transformation of the martensite to the parent phase. Tangents to the forward and reverse transformation peaks during the cooling and heating cycles are constructed to determine the martensite start (M_s), martensite finish (M_f) as well as the austenite start (A_s) and austenite finish (A_f) temperatures, respectively. Transformation temperatures of all the laser deposited samples are tabulated in Table 2.

At the first hand, wide peaks or humps are observed, particularly for the $NiTi_{\_E1}$ alloy as evident from Fig. 4(b). It is noteworthy that *LENS* process implementing lower energy density is associated with formation of thermally induced defects along with improper melting and inhomogeneous microstructure development. It is reported in the previous studies that such non-uniformities leads to sluggish transformation characteristics [10,23]. These could be the reasons for the shallow and less prominent transformation peaks for the $NiTi_{\_E1}$ alloy. On the other hand, higher laser deposition energies for the $NiTi_{\_E2}$ and $NiTi_{\_E3}$ alloys avoid or reduce the chances for these defect generations and homogenizes the microstructure further. Consequently, phase transformation is noted to be prominent and sharper on increasing the laser energies for formation, as observed for the $NiTi_{\_E2}$ and $NiTi_{\_E3}$ alloys. Nevertheless, evidence of single step phase transformation with variation in temperature is observed primarily for the $NiTi_{\_E1}$ and $NiTi_{\_E2}$ alloys.

Table 2
Phase transformation temperatures of $NiTi_{\_E1}$, $NiTi_{\_E2}$ and $NiTi_{\_E3}$ alloys manufactured by *LENS*.

Alloy	A_s (°C)	A_f (°C)	M_s (°C)	M_f (°C)
$NiTi_{\_E1}$	–43.5	23	0	–79
$NiTi_{\_E2}$	–24.5	26	–1.5	–57.5
$NiTi_{\_E3}$	17	52.5	16.5	–24

It is noteworthy that a hint of oscillation or double peak is observed for the $NiTi_{\_E3}$ alloy. Such multi-step peak has been noted in earlier research primarily for the Ni-rich NiTi [40–43]. Occurrence of double peaks in the *DSC* plots for NiTi manufactured by laser based additive manufacturing technique is also documented by Haberland et al. [10]. The studied alloy although not significantly Ni-rich, has a bit higher Ni content in comparison to the equiatomic one. A possibility of occurrence of intermediate R-phase transformation from the parent phase prior to its final conversion to the martensite phase might be a probable reason for such oscillated *DSC* peak, particularly observed for $NiTi_{\_E3}$. However, the transformation is not complete and the peak did not reach the baseline. Hence, any assumptions on this basis could be only hypothetical.

Furthermore, careful scrutiny of the results reported in Table 2 and Fig. 4(b) signify that all the respective transformation temperatures increase for the NiTi alloys manufactured with increasing laser energy densities. This can be primarily attributed to the Ni evaporation with higher energies of the manufacturing [10–12]. It is also evident from

the results that while the M_s temperatures are way below the room temperature for the NiTi$_{_E1}$ and NiTi$_{_E2}$ alloys, that for the NiTi$_{_E3}$ alloy is close to the room temperature. On the other hand, the A_f temperatures for the NiTi$_{_E1}$ and NiTi$_{_E2}$ alloys are just close to or a little lesser than the room temperature. A_f temperature for the NiTi$_{_E3}$ alloy however, is above the ambient temperature. This signifies that at ambient condition, the martensite to austenite conversion completes for the first two alloys. However, for the NiTi$_{_E3}$ alloy, this reverse transformation is only half a way at room temperature leading to the possibility of existence of trace amount of martensite phase. This is further supported by the *XRD* results (Fig. 4(a)). Presence of precipitates also eases the formation and stabilization of the martensite phase [44]. It is noteworthy that the effect of the compositional change on the transformation characteristics of the NiTi alloy is a complex underplay of several factors including precipitate formation, oxygen absorption, Ni evaporation etc. [10–12,44]. All these factors are primarily controlled by the variation in the laser parameters for the *LENS* process.

All the detailed microstructural, phase and thermal analysis for the *LENS* manufactured NiTi alloys reveal that the laser energy for manufacturing affects the microstructural and phase evolution as well as the transformation temperatures of the alloy significantly. The increase in laser energy density reduces the porosity level, as observed for the NiTi$_{_E3}$ alloy. However, existence of trace amount of precipitates at room temperature is noted for this alloy as well. This further influences the phase transformation characteristics of the alloy. All these modifications are certainly expected to alter the mechanical performance of the NiTi alloy as well, which are analyzed and reported next.

3.4. Mechanical behavior study

Additive manufacturing technique is associated with variation in the microstructure throughout the product, as explained in Section 3.1. Hence, studying the corresponding effect in altering the mechanical properties of the materials is of utmost importance. To appreciate this, systematic indentation study has been performed on all the regions and planes, including the front (x–y), side (y–z) and cross-sectional (z–x) planes, as shown in Fig. 1(a). Hardness of all the alloys are investigated using the indentation techniques. Corresponding elastic moduli of the alloys are also estimated from the instrumented indentation tests. It is evident from such study that the hardness values of the cross-section alter significantly in comparison to the other planes. Moreover, the top section of the plane reveals higher hardness with respect to that of the bottom section. This is primarily due to the difference in microstructural evolution in the two regions, as explained in Section 3.1. While repeated heat treatments/aging for the bottom region leads to coarsened grains, fast cooled top region exhibits finer grains and therefore higher hardness [34]. The hardness values for all the regions of the front and side planes on the other hand, are noted to vary only nominally. This is owing to the microstructural similarity between these two planes as explained in Section 3.1. Hence, for the representation, the results reported in this section (Figs. 5–8) correspond to that obtained from indenting the middle region of the front plane. To assess both the bulk as well as local properties of the materials and to estimate the indentation size effect, all the macro-, micro- and nano-indentations are performed. A wide range of indentation loads varying over five orders of magnitude (1 mN up to 500 N) are applied for the evaluation process. Attempts were made to rationalize the size effect as well as to appreciate the pseudoelastic characteristics of the *LENS* manufactured NiTi alloys.

3.4.1. Macrohardness

To investigate the mechanical properties of the bulk NiTi$_{_E1}$, NiTi$_{_E2}$ and NiTi$_{_E3}$ alloys, the macro-hardness tests were performed using a self-similar Vickers indenter. Maximum load of 500 N was used initially. It is noted that the hardness of the NiTi alloys produced using different laser energy densities does not vary significantly, as observed from Fig. 5(a).

An average hardness value of ~2.4 GPa is obtained for the NiTi alloys. It is also evident from the post indentation microscopic characterization (Inset of Fig. 5(a)), that a large indention imprint size of ~500 × 500 μm^2 is achieved. Such a large indentation size covers almost all types of grain morphologies which are heterogeneously distributed in the microstructure. Furthermore, macro-indentations are performed with peak loads reduced sequentially up to 50 N. However, no significant variation in the hardness values are observed with alteration in the load levels. Macro-indentation is therefore noted to be free of any size effect and is capable of successfully estimating the hardness of bulk NiTi alloy irrespective of its microstructural and phase inhomogeneity.

3.4.2. Microhardness

Next, instrumented micro-indentation is performed to assess the properties of all the *LENS* manufactured NiTi$_{_E1}$, NiTi$_{_E2}$, and NiTi$_{_E3}$ specimens utilizing lower load levels. It is noteworthy that the instrumented indentation technique, mostly employed in small scale indentation such as micro- and nano-indentation, leads to a precise estimation of a material's elastic modulus along with its hardness. Standard indentation load (P) vs. depth of penetration (h) curves for all the NiTi alloys are obtained from the experiments. Representative micro-indentation P–h curves for the specimens are presented in Fig. 5(b).

Hardness, H and elastic modulus, E of the alloys are estimated from such curves using the Oliver–Pharr method [45,46]. Hardness is estimated from the projected contact area (A_p) of the indents and P as per the following relation:

$$A_p = 3\sqrt{3}h_c^2 tan^2\theta;\ H = \frac{P}{A_p} \tag{2a}$$

where, h_c is the contact depth of penetration and θ is the face angle of the geometrically self-similar indenter.

Elastic moduli of the test material, is determined from the P–h curve using the slope of the unloading part a per the following relation:

$$\frac{1}{E_r} = \frac{1-\nu^2}{E} + \frac{1-\nu_i^2}{E_i} \tag{2b}$$

where, ν and E are Poisson's ratio and elastic modulus of the NiTi alloy. ν_i and E_i are Poisson's ratio and elastic modulus of the diamond indenter. The values of ν_i and E_i are considered as 0.07 and 1140 MPa, respectively [47]. The reduced elastic modulus, E_r on the other hand, is estimated from the equation involving S i.e. the stiffness or slope of the unloading curve at maximum displacement ($S = dP/dh$) and A_p as $E_r = \frac{\sqrt{\pi}}{2}\frac{S}{\sqrt{A_p}}$ [28,29].

It is also important to consider that statistically significant number of indentations are performed for all the alloys at each load levels to rule out the scatter lead by different factors, the prime being heterogeneity in the microstructure and phase as well as presence of precipitates [48,49]. Nevertheless, the indent impressions for micro-indentations are also fairly large (50 × 50 μm^2) covering more than one or two grains at the least. This provides a scope to estimate the properties of the material irrespective of the effect of grain size and morphologies. Variation of H and E for the NiTi$_{_E1}$, NiTi$_{_E2}$ and NiTi$_{_E3}$ alloys with varying load levels are presented in Fig. 5(c). Average elastic modulus of the *LENS* manufactured NiTi alloys is noted to be ~65 GPa (Fig. 5(c)). The value matches reasonably well with the standard elastic modulus of NiTi [46,50]. A nominally lower value however corresponds to the porous and as processed microstructure produced by the *LENS* process. Hardness of the alloys, on the other hand, turn around to be ~2.9 GPa on application of micron level loads. It is evident from the plot (Fig. 5(c)) that the H and E values does not vary significantly with variation in the indentation load levels. A nominally increased H value is obtained for the NiTi$_{_E3}$ alloy, which however is still within the error limit. Presence of trace amount of precipitates along with the martensite content in the alloy, as evident from the microstructural and phase investigation, could be the possible reason for that [44,51,52].

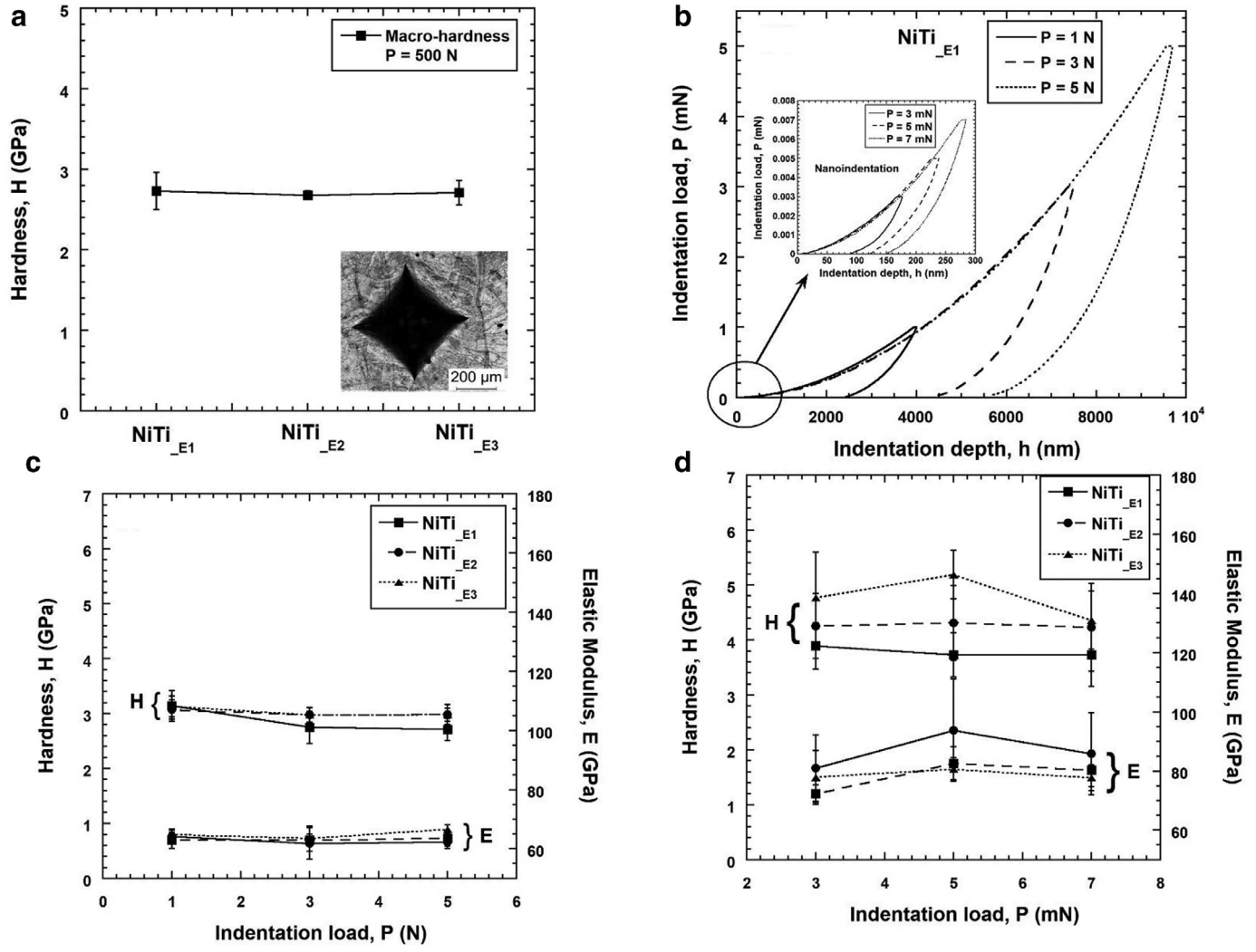

Fig. 5. (a) Variation in hardness (H) of NiTi$_{_E1}$, NiTi$_{_E2}$ and NiTi$_{_E3}$ alloys at a representative indentation load, assessed from macro-Vickers indentation tests. Optical micrograph showing a representative indentation is presented at the inset. (b) Representative P–h curves for the NiTi$_{_E1}$ alloy obtained from the micro- and nano-indentation experiments. Inset highlights the representative nanoindentation P–h curves. Fig. 5 variation in H and E at different indentation load levels for the NiTi$_{_E1}$, NiTi$_{_E2}$, NiTi$_{_E3}$ alloys on (c) micro-indentation and (d) nano-indentation experiments.

3.4.3. Nanoindentation

Further to the macro- and micro-indentations, instrumented nanoindentations are performed using Berkovich indenter tip to analyze the properties of all the *LENS* manufactured NiTi alloys at even smaller scale. Load levels of 3, 5 and 7 mN are used for the study. Representative P-h curves for the NiTi$_{_E1}$ alloy is presented in Fig. 5(b) and is highlighted at the inset. Variation of H and E for all the NiTi$_{_E1}$, NiTi$_{_E2}$, and NiTi$_{_E3}$ alloys with varying load levels in the nano-scale are presented in Fig. 5(d). Both H and E values of NiTi alloy in general as estimated from the nanoindentation of NiTi alloys match reasonably well with the literature [53]. The values for the individual alloys are not noted to alter with varying load levels. A careful scrutiny of the nanoindentation results however, reveals a notable variation in the trend of modulus and hardness for the NiTi alloys manufactured with different laser energy densities. It is evident from the figure (Fig. 5(d)) that the alloy manufactured with highest laser energy density, NiTi$_{_E3}$, exhibits lower modulus but higher hardness (by ~20%) in comparison to the NiTi$_{_E1}$ alloy. This is particularly true at lower levels of 3 and 5 mN. A similar trend, although less prominent is apparent from the micro-indentation results as well and hence represents a genuine fact.

It is observed that such an increase in H for the NiTi$_{_E3}$ alloy can be justified based on the microstructural and phase analysis of such alloy. It is evident from the *TEM* images and *XRD* plots (Fig. 2(c) and 4(a)) that unlike the other two alloys, NiTi$_{_E3}$ consists of a minor fraction of Ti_2Ni precipitates in the microstructure. It is noteworthy that such precipitates having significantly higher hardness in comparison to the B2 matrix, enhances the hardness of the system [35,36,38,50,53]. Additionally, possibility of occurrence of martensite phase in the structure can also affect the hardness and modulus variation of the NiTi$_{_E3}$ alloy. The monoclinic phase has significantly higher hardness as well as lower elastic modulus in comparison to that for the austenite phase [53–57]. Nevertheless, such variation in hardness for NiTi$_{_E3}$ alloy owing to the presence of precipitates and second phase can only be appreciated using small scale indentation. This is primarily due to the presence of very low volume fraction of the particles in the NiTi$_{_E3}$ alloy. Characterizing through macro-indentation and thereby involving larger indentation cross sectional area and volume beneath the indents however is not apt to ascertain the role played by the nominal presence of such phase.

3.4.4. Indentation size effect

The results obtained from the indentation experiments considering all the different load levels are carefully scrutinized next. It is observed from the individual macro-, micro- as well as nano-indentations that

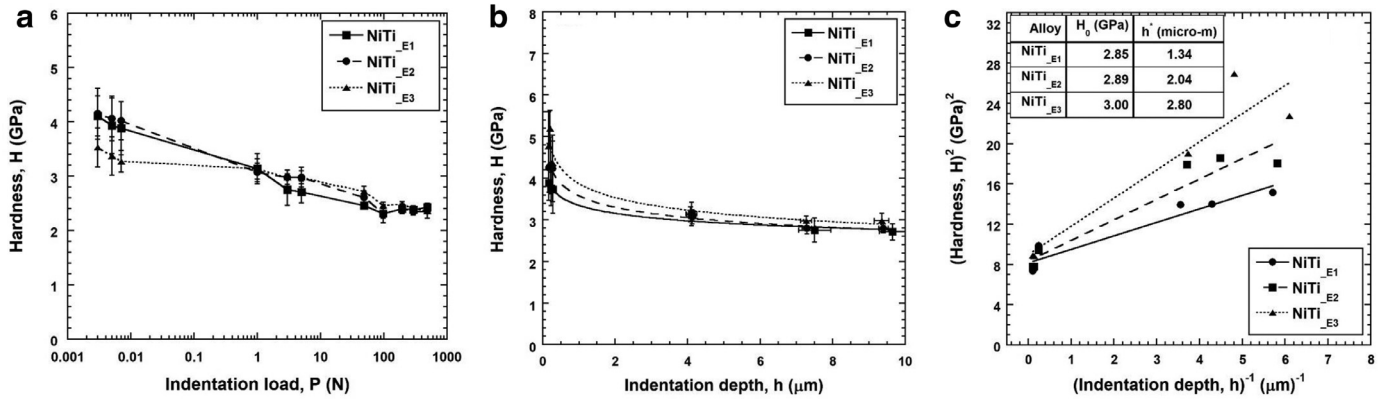

Fig. 6. Variation of hardness with (a) indentation load (P) and (b) depth of penetration (h). A sharply decreasing slope indicates occurrence of indentation size effect. (c) Variation of the square of hardness (H^2) w.r.t. the inverse of depth of penetration (h^{-1}) curve. The values of H_o and h^* for all the alloys are estimated from the curve.

fine tuning of the load levels within the respective ranges do not alter the hardness of the alloys significantly. However, the average values of hardness of the *LENS* manufactured NiTi alloys, as estimated from micro-indentation is noted to be higher (~2.9 GPa) in comparison to that assessed from macro-indentation (~2.4 GPa). Similarly, nano-hardness (~4.2 GPa) is noted to be even higher compared to the micro-hardness. Significant enhancement in H of the NiTi alloys by ~75% is therefore observed on reducing the indentation load levels by more than five orders of magnitude during macro- to nano-indentation. This is also evident from Fig. 6(a). The variation of mean values of H for the *LENS* manufactured NiTi alloys with indentation depth of penetration, h is presented in Fig. 6(b). It is further noted that on decreasing the maximum indentation depth, h_{max} levels from the micro- to the nano-levels i.e. from ~10 μm to ~150 nm, H values vary largely (by ~67%).

Such a trend of increasing hardness with decrease in indentation load or depth of penetration is considered as the indentation size effect (*ISE*). The study by Nix and Gao is pioneer in this field to explain the detailed mechanisms of *ISE* [49,58–62]. According to that, on indenting the specimen surface, geometrically necessary dislocations (*GNDs*) generate within the indentation volume beneath the indenter tip. These *GNDs* primarily account for the shape change associated with the indent impression imprinted on the specimen surface. This further corresponds to prevalence of a strain gradient within the indentation volume. Smaller the indentation depth, larger is the strain gradient and hence larger is the density of *GNDs*. Such high dislocation density leads to enhanced hardening at smaller indentation depth [58,63–65]. It is noted that H and h are related to each other as per the following equation:

$$\frac{H}{H_0} = \sqrt{1 + \frac{h^*}{h}} \tag{3}$$

where, H_0 is the hardness at infinite indentation depth. In other words, it is the hardness that would arise from merely the statistically stored dislocations (*SSDs*) in absence of *GNDs*. h^*, on the other hand, represents the depth dependence of hardness. It is a characteristic depth that depends on the shape of the indenter, shear modulus and H_0 as well [58,63,66].

To carefully assess the *ISE* in the *LENS* manufactured NiTi alloys, a plot of square of hardness vs. reciprocal of indentation depth is presented (Fig. 6(c)). Linear nature of the variation of H^2 vs. h^{-1} for the NiTi alloys do signify that indentation size effect is active for this material. Quantification of *ISE* for the alloys is further performed on the basis of the curve. The value of H_0 is obtained from the intercept of the linear variation with its ordinate. The slope of the line, on the other hand, signifies h^*. For all the alloys, H_0 values are noted to be more or less consistent and attains a mean value of 2.91 GPa. The values are tabulated and presented at the inset of Fig. 6(c).

Such a value of H_0 is also observed by Abbas et al. for NiTi alloy [56]. A nominally higher value of H_0 for the NiTi$_{_E3}$ alloy in comparison to the other two alloys signify higher hardness at infinite depth for this alloy manufactured with the highest laser energy density. It is therefore evident that the hardness dictated by the *SSDs* is higher for the NiTi$_{_E3}$ alloy. This could be owing to the presence of trace amount of precipitate as well as martensite phase in the microstructure of NiTi$_{_E3}$ alloy, both of which enhances the hardness of the alloy [53]. This was also apparent from the nanoindentation results as well (Fig. 5(d)). The highest value of h^* for the NiTi$_{_E3}$ alloy further confirms that the depth dependence of hardness is maximum for this alloy. Reduction in the pseudoelasticity could also be a possible reason for such behavior. This factor is clarified further in the next section.

3.4.5. Spherical nanoindentation and indentation stress–strain behavior

The microstructural investigation corroborated with the indentation study signify that the alteration in the processing parameters of *LENS* do affect the microstructure generation and phase evolution of NiTi. However such microstructural and crystallographic modifications lead to only nominal increase in the hardness of NiTi$_{_E3}$ alloy owing to the presence of trace amount of Ti_2Ni precipitates as well as room temperature martensite phase in the alloy. Nevertheless, it is noteworthy that the indentation experiments performed with the conventional sharp Vickers or Berkovich indenter tips are capable of precisely evaluating the mechanical properties in terms of hardness and elastic modulus of a material. However, such sharp tips are not appropriate to assess the pseudoelastic behavior of the alloy. This is particularly so as the indentation volume beneath the sharp indenter tip of diameter ~100–200 nm is dominated by the dislocation mediated plasticity. These *GNDs* superpose the reversible phase transformation i.e. *SIMT* based pseudoelasticity in NiTi. Such recoverable pseudoelastic behavior of an alloy however can be better appreciated using spheroconical (commonly known as spherical) indenter tip with a comparatively blunt tip of diameter around two orders of magnitude higher than that of Berkovich indenter tip. A schematic representation of the deformation zones within the indentation volumes beneath a Berkovich and a spherical tip is presented in Fig. 7(a). For a pseudoelastic NiTi alloy, primarily three deformation zones develop within that volume – namely plastic, pseudoelastic and elastic marked as '*A*', '*B*' and '*C*', respectively [67]. Dislocation based plasticity is more pronounced in the plastic region – '*A*' whereas the stress induced phase transformation and the associated pseudoelasticity is reflected in the mid-zone – '*B*'. Zone '*C*', or the far most zone from the indenter tip, however is free from dislocation or *SIMT* based activities. '*C*' therefore represents the elastic zone with fully recoverable deformation. It is clearly evident from the schematic (Fig. 7(a)) that the pseudoelastic activity – zone '*B*', is quite pronounced in case of the indentation volume beneath the

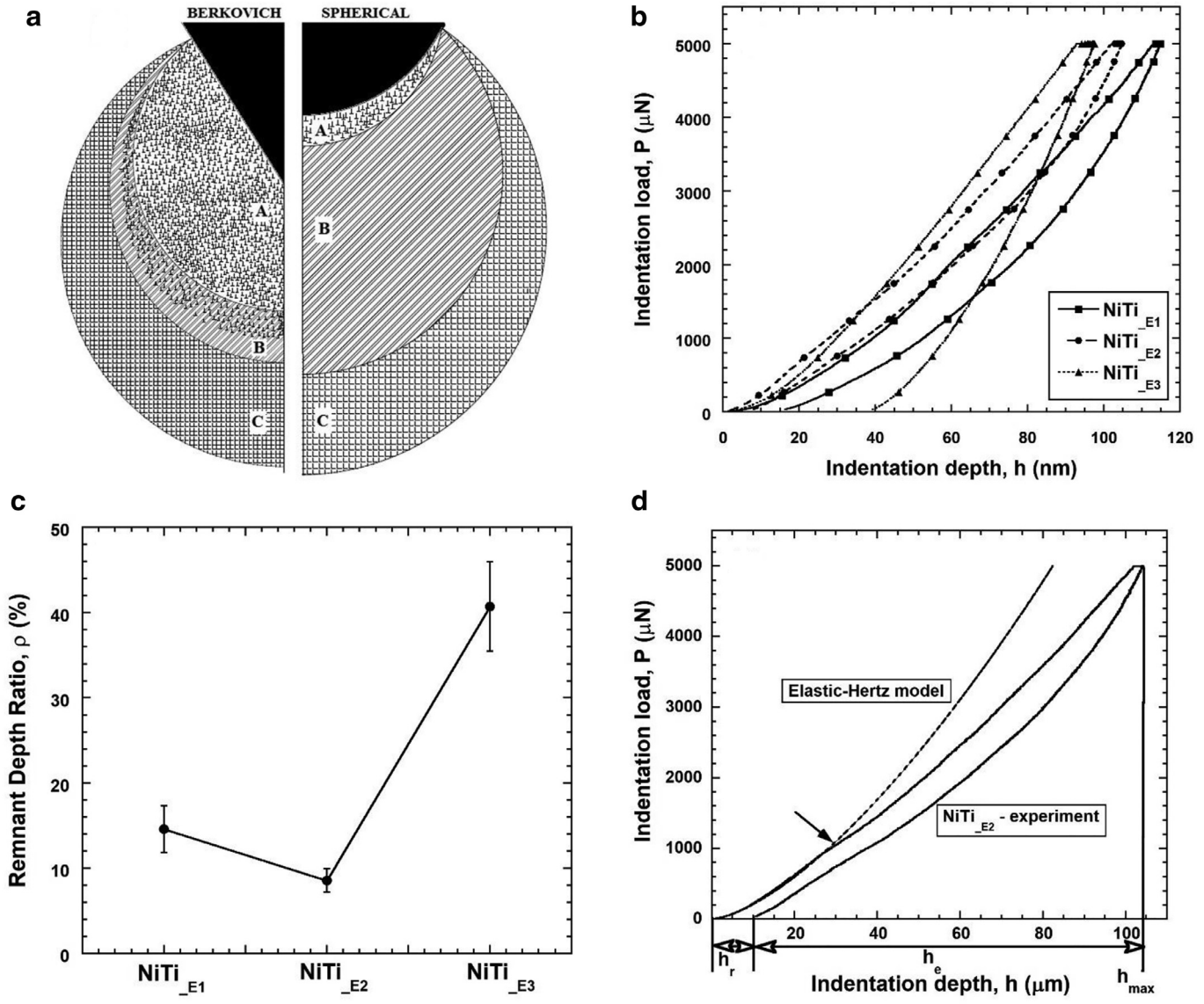

Fig. 7. (a) Schematic representation of deformation mechanism beneath the Berkovich and spherical indenter tip for a pseudoelastic NiTi alloy. In the figure, the regions (*A*), (*B*) and (*C*) represent the consecutive zones for dislocation activity i.e. plasticity; stress induced martensite activity i.e. pseudoelasticity and elastic deformation, respectively. (b) Representative *P–h* curves and (c) variation of remnant depth ratio (ρ) for the $NiTi_{\_E1}$, $NiTi_{\_E2}$ and $NiTi_{\_E3}$ alloys. (d) Representative *P–h* response of $NiTi_{\_E2}$ as obtained from the nanoindentation experiment as well as the corresponding curve based on the Hertz equation for an elastic deformation.

spherical tip (right side of the schematic). The scope to precisely assess pseudoelasticity therefore is better while indenting with a spherical tip.

Representative *P–h* curves for all the *LENS* manufactured NiTi alloys, nanoindented with spherical indenter tip of diameter 40 μm are presented in Fig. 7(b). Although the difference in the shapes of the *P–h* curves generated by sharp Berkovich and blunt spherical indenter tips are apparent from Figs. 5(b) and 7(b), it is better quantified from the value of the remnant depth ratio (ρ). ρ of a specimen undergoing instrumented indentation signifies the pseudoelastic recovery of the material. ρ is quantified from its *P–h* curve as the ratio of h_r to h_{max} (Eq. (4)).

$$\rho = \left(\frac{h_r}{h_{\max}}\right) \times 100. \tag{4}$$

While a low value of ρ (≤10%) signifies pseudoelasticity, a higher value corresponds to pronounced plastic deformation [68–73]. Variation of *RDR* at a representative load of 5 mN for the $NiTi_{\_E1}$, $NiTi_{\_E2}$ and $NiTi_{\_E3}$ alloys are shown in Fig. 7(c). As expected, the one possessing trace amount of precipitates as well as martensite phase, i.e. $NiTi_{\_E3}$ alloy exhibits a lower strain recoverability. Highest ρ value of 41 ± 5% is noted for this alloy which is far beyond the acceptable limit of 10% for a typical pseudoelastic alloy. This is also evident from its *P–h* curve (dotted curve in Fig. 7(b)) revealing lesser recoverable deformation or in other words, higher amount of permanent deformation. On the other hand, the *P–h* curves for the $NiTi_{\_E1}$ and $NiTi_{\_E2}$ alloys yield ρ values of 15 ± 3 and 9 ± 1, respectively. Such lower ρ values are quite close to the targeted value. It is noteworthy that the ρ value of $NiTi_{\_E1}$ although is nominally higher than 10%, has significant scatter in the data. Rather, the $NiTi_{\_E2}$ alloy shows the optimum targeted ρ value <10%. This signifies that the processing condition or the laser energy density for producing the $NiTi_{\_E2}$ alloy is ideal for producing the one with the best pseudoelastic recoverability.

It is noteworthy that the alteration in the laser energy densities for the *LENS* process is not reflected in significantly affecting the conventional mechanical properties i.e. the hardness and elastic modulus of the NiTi alloys. The self-similar Berkovich indenter tip with its sharp

tip geometry and higher remnant plastic deformation, on the other hand, yields a higher and constant value of ρ (~65%) irrespective of the load applied or indentation depth achieved. This is also evident from Fig. 5(b) [70,73,74]. It is therefore uniquely apparent from the results of the spherical nanoindentation that the pseudoelastic characteristics of the material, which primarily depends on its phase structure, modify owing to such change in the additive manufacturing parameters.

It is noteworthy that apart from precisely estimating the recoverability of the NiTi specimens, the *P-h* responses of the alloys also indicate the exact applied load required for the onset of pseudoelasticity. This can be better appreciated considering the classical Hertz theory for elastic and frictionless material [45,75]. According to Hertz theory, indentation load, P is related to the effective or reduced elastic modulus, E_r of the material as well as the effective indenter tip radius, R_{eff} along with the corresponding elastic indentation depth, h_e as per the following equations:

$$P = \frac{4}{3} E_r R_{eff}^{\frac{1}{2}} h_e^{\frac{3}{2}} \tag{5a}$$

$$\frac{1}{R_{eff}} = \frac{1}{R_s} + \frac{1}{R_i} \tag{5b}$$

In the above equations, R_i and R_s denote radius of indenter tip and radius of curvature on the sample surface, respectively. It is noteworthy that for elastic loading on a flat surface, R_s approaches to infinity. Hence, effective radius turns out to be same as the indenter tip radius, R. Furthermore, for a psueudoelastic alloy having significant depth recovery, h_e corresponds almost to the h_{max}. For considering the E_r in Eq. (5), it is important to appreciate that E of the NiTi alloy (Eq. (2b)) is dependent on the volume fraction of the austenite and martensite phases, at any point. E_r is further controlled by the respective modulus of these constituent phases, which however are significantly different [50,76]. It is noteworthy that *SIMT* of NiTi commences almost initially as the specimen is subjected to indentation. This primarily is associated with the sharp strain gradient within the indentation volume as explained through Section 3.4.4 and Fig. 7(a). Hence, mixture of phases is expected to exist within the indentation volume at any instance. Considering the complexity to precisely assess the phase fraction of NiTi as the indentation progresses, an average value of the elastic modulus of both the phases are considered for this study.

To further illustrate the importance of Hertz equation to appreciate pseudoelasticity of a material, experimental *P–h* response of a representative alloy, NiTi$_{_E2}$ nanoindented using spherical indenter tip radius of 20 μm and P of 5 mN is presented in Fig. 7(d). In addition, schematic representation of the *P–h* response of the material based on the Hertz equation (dashed line) is also superimposed in the plot. The later signifies the perfectly elastic deformation behavior of the alloy undergoing the same applied loading scenario.

It is evident from the figure that the two plots deviate at a particular load as indicated by an arrow. This critical load signifies the one necessary to alter the deformation behavior of the subjected material from elastic to non-elastic such as pseudoelastic or plastic. It is evident from the unloading part of the *P–h* curve for NiTi$_{_E2}$ (solid curve in Fig. 7(d)) that significant load recovery prevails for this material. The critical load (arrow) in this case therefore, represents the load required for the onset of pseudoelastic deformation.

It is important to note that all the parameters to assess the mechanical performance of a material are better appreciated from its stress–strain behavior. The spherical nanoindentation *P–h* response of the *LENS* manufactured NiTi alloys is therefore converted to the corresponding indentation stress–strain (σ_{ind}–ε_{ind}) curves. Such a complementary study provides a scope to assess the nature of the transformation mechanism in the NiTi alloys. The indentation stress, σ_{ind} and indentation strain, ε_{ind} developed during spherical nanoindentation are estimated according to the following relations:

$$\sigma_{ind} = E_{eff} \cdot \varepsilon_{ind} \tag{5c}$$

$$\sigma_{ind} = \frac{P}{\pi a^2},\ \varepsilon_{ind} = \frac{h_{max}}{2.4a} \tag{5d}$$

where h_{max} represents the maximum depth of indentation. a on the other hand, signifies the radius of the contact boundary of the indentation volume and is expressed by the relation $a=\sqrt{(R_{eff} h_e)}$. In this study, R_{eff} is assumed to be same as the indenter tip radius and h_e is considered to be equivalent to h_t. It is noteworthy that such assumptions are particularly valid for NiTi that yields significant elastic as well as additional pseudoelastic recoverability.

The representative $\sigma_{ind} - \varepsilon_{ind}$ curves for NiTi$_{_E1}$, NiTi$_{_E2}$, and NiTi$_{_E3}$ alloys are presented in Fig. 8.

It is apparent from the plots that the $\sigma_{ind} - \varepsilon_{ind}$ curves for the alloys, NiTi$_{_E1}$ and NiTi$_{_E3,}$ are distinctly different from each other as well as from the NiTi$_{_E2}$ alloy. Elastic recovery is mostly prominent for the case of the NiTi$_{_E1}$ alloy. Consequently, although its strain recoverability is noted to be quite high, the corresponding $\sigma_{ind} - \varepsilon_{ind}$ curve does not show any distinct plateau region or significant change in the slope. This signifies absence or rare occurrence of *SIMT* in the NiTi$_{_E1}$ alloy. This is also evident from the *P-h* curve y and low value of ρ for the alloy (Fig. 7(b) and (c)).

Interestingly, it is noted that the $\sigma_{ind} - \varepsilon_{ind}$ curve for the NiTi$_{_E2}$ alloy (Fig. 8(b)) corresponds to that of a typical pseudoelastic behavior. The plateau region in the graph along with a significant strain recovery confirms the activity of reversible *SIMT* in the material. The stress required for the onset of martensitic transformation for this alloy, $\sigma_{ind\text{-}tr}$ is estimated to be 527.6 ± 24 MPa. Values of transformation stress in the similar range are also noted by other researchers [77]. The nature of the indentation stress–strain behavior of the NiTi$_{_E2}$ alloy resembles well with that observed by Gall et al. on studying the compressive response of the NiTi [78]. Similar behavior is also apparent from the bulk scale tensile testing of the alloy, as presented in the next sub-section.

Moreover, the $\sigma_{ind} - \varepsilon_{ind}$ curve for the NiTi$_{_E3}$ alloy (Fig. 8(c)) reveals features of conventional plastic material behavior. Careful scrutiny of the graph highlights absence of pseudoelastic plateau. It is clearly visible that the amount of recoverable strain is quite low in the NiTi$_{_E3}$ alloy in comparison to that of the NiTi$_{_E1}$ and NiTi$_{_E2}$ alloys. This is in line to the crystallographic and phase analysis of the alloys as discussed in Section 3.2 and 3.3 as well as Fig. 4.

3.4.6. Tensile properties

The insight developed from the indentation study, on the localized mechanical properties of the *LENS* manufactured NiTi alloys is extrapolated further to their global performances by performing conventional tensile tests. It is mentioned in Section 3.1 that the microstructure of the *LENS* manufactured alloys change particularly along the cross-section i.e. *x–z* planes in comparison to that of the other planes. This poses a possibility to alter the localized properties at different planes. For the tensile testing, however, uniaxial loads are applied along the build direction. Hence, such a characterization is expected to estimate a more or less generalized set of properties taking into consideration all the non-homogeneities. Representative engineering stress–strain characteristics of the alloys are presented in Fig. 8(d).

It is apparent from the plots that the behavior of NiTi$_{_E1}$ and NiTi$_{_E3}$ are quite comparable. For these two alloys, 0.2% offset stress amount to ~540 MPa and ~600 MPa, respectively. No trace of pseudoelasticity in terms of strain plateaus are however apparent from the respective stress–strain curves of these alloys. This indicates that the above mentioned offset stresses correspond to the yield strengths of the NiTi$_{_E1}$ and NiTi$_{_E3}$ alloys. Highest ultimate tensile stress of ~780 MPa associated with lowest ductility of ~4.5% is observed for the alloy produced with the highest laser energy density i.e. NiTi$_{_E3}$ alloy. This observation synchronizes with that obtained from the indentation study.

Interestingly, unlike the other two alloys, the engineering stress–strain curve for NiTi$_{_E2}$ alloy shows significant plateau strain that extends up to ~10% as indicated with an arrow. This nominally constant

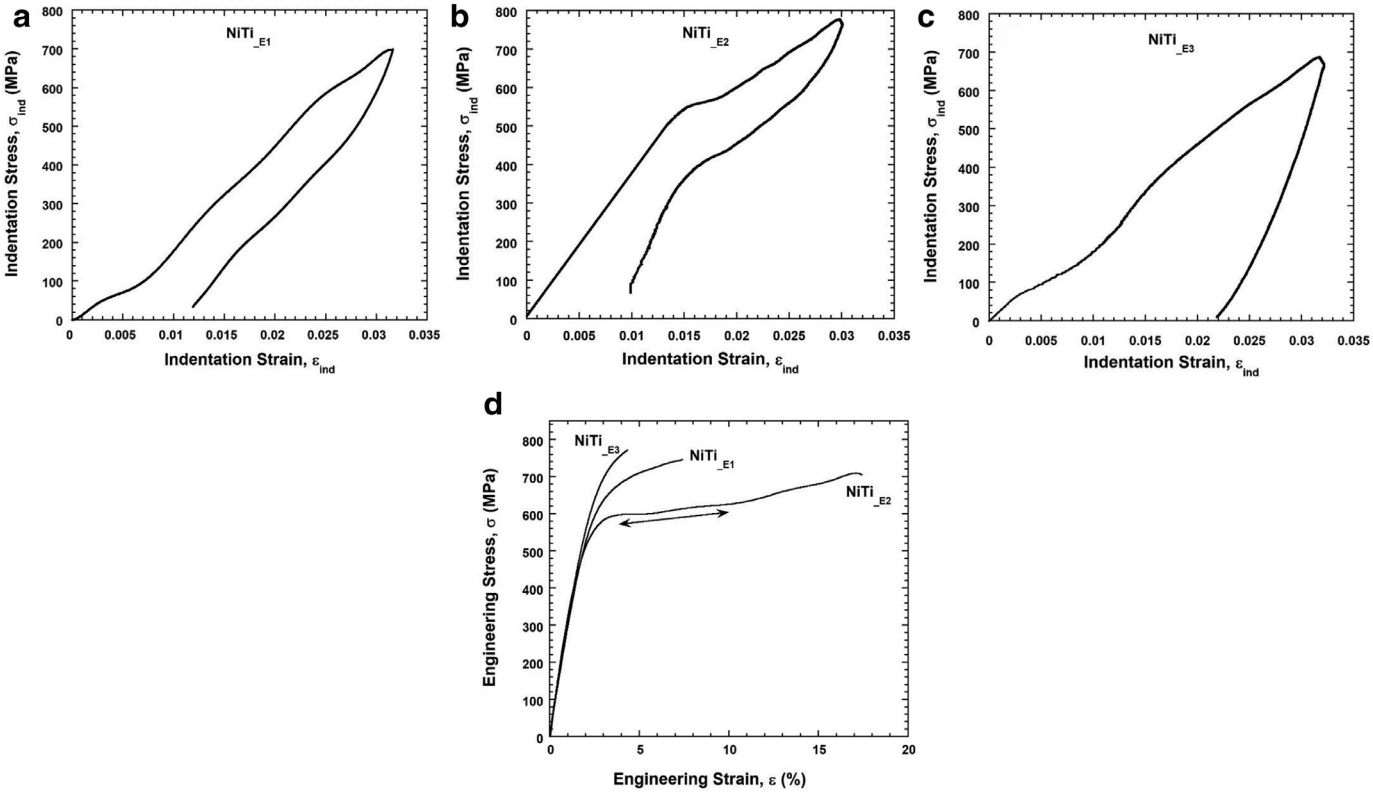

Fig. 8. Indentation stress–strain curve for (a) $NiTi_{\_E1}$, (b) $NiTi_{\_E2}$ and (c) $NiTi_{\_E3}$ alloys. (d) Engineering stress–strain curves for $NiTi_{\_E1}$, $NiTi_{\_E2}$ and $NiTi_{\_E3}$. Plateau strain is observed for $NiTi_{\_E2}$ alloy.

stress deformation indicates for the occurrence of stress induced martensitic transformation in the alloy. Hence, the 0.2% offset stress in this case is considered as the martensitic transformation stress, σ_{tr}, which amounts to ~500 MPa. Corresponding transformation strain, ε_{tr}, turns to ~2%. Similar deformation characteristic for $NiTi_{\_E2}$ alloy is evident from the spherical nanoindentation studies (Fig. 8(b)). Moreover, σ_{tr} for $NiTi_{\_E2}$ alloy matches reasonably well with that obtained from the respective indentation stress–strain curves, $\sigma_{ind\text{-}tr}$ (~527 MPa). Nominally higher value of $\sigma_{ind\text{-}tr}$, on the other hand, account for the tri-axial stress state along with small scale deformation associated with nanoindentation [5,79].

Nevertheless, apart from the stress induced phase transformation and the corresponding plateau in the stress–strain curve, pseudoelasticity of NiTi is particularly dictated by its capability to largely recover the strain generated during deformation. This could be only realized provided the *SIMT* activity in NiTi is reversible. Hence, to estimate and analyze the strain recoverability and the related pseudoelasticity of the NiTi alloys manufactured by *LENS*, it is necessary to perform the cyclic tensile tests of the alloys [80]. In this case, tensile specimens were loaded continuously up to a certain maximum strain, ε_{max} followed by unloading the specimens back to 0 MPa. It is noteworthy at this point that the tensile test results presented in Fig. 8(d) is estimated in absence of an extensometer or strain gage. All the strain values estimated are therefore nominally higher. Considering this, a lower value of ε_{max} as 1.5% is applied for the cyclic tensile tests. Such lower value of ε_{max} avoids the occurrence of significant plasticity, if any, within the specimens. Representative engineering stress–strain curves obtained from the cyclic tensile tests for all the alloys are presented at Fig. 9(a). Considering that the cyclic tensile tests are performed within a significantly lower strain range, nominal variation in the respective elastic slopes for the alloys are noted.

As expected, the stress–strain values obtained during the loading sequence of the cyclic tensile tests (Fig. 9(a)) match reasonably well but not exactly with that of the conventional tensile tests (Fig. 8(d)). This is particularly owing to the use of extensometer for the cyclic tensile tests. Up on complete unloading, the existent remnant or minimum strains, ε_{min} for all the $NiTi_{\_E1}$, $NiTi_{\_E2}$, and $NiTi_{\_E3}$ alloys are estimated from the extensometer reading and the corresponding strain recoverabilities of the alloys are assessed. It is apparent from the graphs (Fig. 9(a)) that all the alloys recover major part (~92 ± 2%) of the strain, unlike that of other conventional metallic systems. This is evident from the change in slope of the unloading curve instead of following the elastic unloading [81]. The study therefore reveals that at lower strain levels (1.5%), all the NiTi alloys manufactured by *LENS* do exhibit reversible *SIMT* leading to higher pseudoelasticity. However, it is further evident from the graphs that the strain recoverability is nominally higher (~97 ± 1%) for the $NiTi_{\_E2}$ alloy (blue curve). This signifies that pseudoelasticity is certainly higher for this alloy in comparison to the other NiTi alloys, manufactured by *LENS* using different processing parameters.

To gain further insight on the forward and backward phase transformation behavior for all the alloys, the overall strains generated in the gage sections of the specimens, as estimated by the extensometer are being complemented by *DIC* analysis. The later reveals the strain distribution throughout the central part of the gage section of the specimens, as the loading and unloading progresses. The variation in the strain generated within the targeted regions are appreciated by the color coded movies or plots captured at different time frames. Representative color coded strain distribution images for the alloys, captured at ε_{max} and ε_{min} are presented in Fig. 9(b) and (c), respectively.

It is apparent from the figures that although the ε_{max}, as estimated by the extensometer reading, amounts to 1.5%, it is not uniformly distributed throughout the gage sections. This is in line with the observation made by various research groups [82–85]. Their studies have shown evidences for inhomogeneous deformation and formation of localized deformation bands while tensile testing pseudoelastic NiTi. Similar non-uniform strain distribution is noted from the present study as

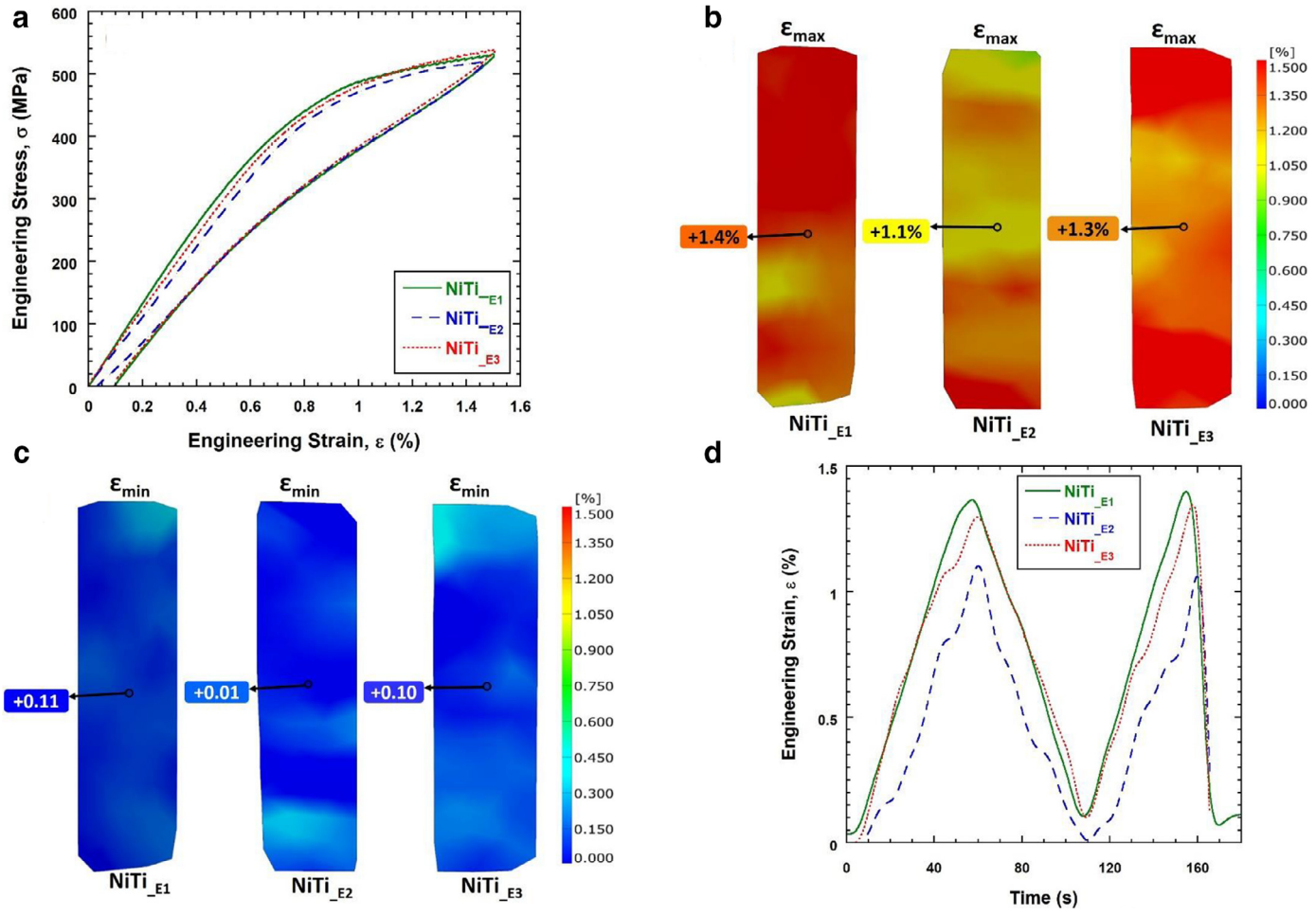

Fig. 9. (a) Engineering stress–strain curves for $NiTi_{\_E1}$, $NiTi_{\_E2}$ and $NiTi_{\_E3}$ alloys as obtained from the cyclic-tensile tests. Increased recoverability is observed for $NiTi_{\_E2}$ alloy. (b) Color coded strain variation within the central gage sections of the $NiTi_{\_E1}$, $NiTi_{\_E2}$ and $NiTi_{\_E3}$ specimens on application of overall maximum tensile strain, $\epsilon_{max} = 1.5\%$. (c) Color coded strain variation within the central gage section of the specimens on complete unloading, leading to remnant strain, ϵ_{min}. Non-uniform strain distribution is apparent for all the alloys. Lowest local ϵ_{max} and ϵ_{min} values are noted for $NiTi_{\_E2}$ alloy. (d) Variation of strain with time at the local central point on the tensile specimens marked in (b) and (c), quantified by *DIC*. Lower strain is achieved in $NiTi_{\_E2}$ alloy at this point throughout the deformation. Lower remnant deformation is apparent from the blue dashed curve on unloading leading to highest recoverability. (For interpretation of the references to colour in this figure legend, the reader is referred to the web version of this article)

well, for all the *LENS* manufactured NiTi alloys, which could lead to nominal amount of plasticity locally, even at such low strain. This is evident from the finite value of ϵ_{min}. However, no particular trend in the strain variation amongst the different NiTi alloys is noted. To account for the generalized strain within the gage section of the tensile specimen, a representative point is chosen at the central part of the specimen (as marked by a circle) to quantify the local strain in all the different NiTi alloys. The local point selection is based on the standard protocol for characterization. It is evident from Fig. 9(b) that while higher applied strain, ϵ_{max} of ~1.5% is noted to prevail, particularly near to the top and bottom edges for the selected region, the central part shows a lighter shade signifying reduced strain. It is quantified that at the selected point, ϵ_{max} values reach lower positive strains of ~1.4%, 1.1% and 1.3% for the $NiTi_{\_E1}$, $NiTi_{\_E2}$ and $NiTi_{\_E3}$ alloys, respectively. Up on unloading back to zero stress, the residual strain values are also noted to vary non-uniformly throughout the selected area in the gage section. It is indicated in Fig. 9(c) that the residual ϵ_{min} values turn up to 0.11, 0.01 and 0.10% for the $NiTi_{\_E1}$, $NiTi_{\_E2}$ and $NiTi_{\_E3}$ alloys respectively. The ϵ_{min} value for $NiTi_{\_E2}$ alloy is therefore noted to be the least thereby inferring occurrence of superior reversible deformation and pseudoelasticity indeed for this alloy. Strain recovery for $NiTi_{\_E1}$ and $NiTi_{\_E3}$ at the selected point amount to ~93% whereas that for $NiTi_{\_E2}$ reaches to a value as high as ~99%.

To commemorate the quantification of the local strain, variation of ϵ with time at the selected central point is presented in Fig. 9(d). It is apparent from the plots that the peak strain signifying, ϵ_{max} as well as the residual strain, ϵ_{min} achieve the lowest values for $NiTi_{\_E2}$ alloy in comparison to the other alloys. It is further apparent from the plots that the localized strains reach a lower value for this alloy (blue dashed curve in Fig. 9(d)) throughout the loading and unloading stages of the cycles. Consequently reduced possibilities of permanent deformation and increased scopes for reversible deformation, reflected as lower residual strain is evident for this alloy [2]. Although, assessing pseudoelastic characteristic of an alloy from its localized deformation behavior may not be appropriate, the cyclic tensile tests and the corresponding strain measurement using extensometer and *DIC* analysis do indicate for improved pseudoelasticity for $NiTi_{\_E2}$ alloy. It is therefore apparent from the study that higher pseudoelasticity of $NiTi_{\_E2}$ alloy is reflected both locally as estimated by nanoindentation and *DIC* and globally, measured by conventional tensile test and extensometer.

In connection to this prime observation, higher strain recoverability of $NiTi_{\_E2}$ alloy with respect to that of $NiTi_{\_E1}$ alloy mandates a clear

justification in this regard. This is particularly considering the fact that both these alloys consist of fully austenite phase at room temperature (Fig. 4(a)). Hence, both $NiTi_{\_E1}$ and $NiTi_{\_E2}$ alloys stand fair chances for *SIMT* up on indentation or tensile loading and therefore to reveal the corresponding pseudoelasticity. However, careful scrutiny of the phase transformation behavior of the alloys (Fig. 4(b)) signifies that the martensitic transformation peaks are sharper in case of $NiTi_{\_E2}$ in comparison to that for $NiTi_{\_E1}$ alloys. This implies that the conversion of austenite to martensite is energetically more favorable for the $NiTi_{\_E2}$ alloy. The austenitic transformation peaks shows a similar pattern for this alloy thereby revealing higher pseudoelasticity for the $NiTi_{\_E2}$ alloy.

It is important to note that such change in mechanical performance of the NiTi alloy is critical particularly for applications prone to cyclic loading. The functional fatigue for the pseudoelastic NiTi in that case will affect the overall performance of the alloy.

4. Concluding remarks

NiTi based shape memory alloys are prepared by additive manufacturing method as per the laser engineered net shaping technique. The role of process parameters such as laser scan speed, power as well as energy density in modifying the microstructure, phase evolution as well as mechanical properties of the alloys are systematically investigated along the different planes and regions of the product. Microstructures and properties of the front and side planes are noted to resemble with each other quite well and are further characterized thoroughly. Signatures of the layer by layer deposition process are evident from the microstructure. Grains of different sizes and morphologies are noted to form accordingly. The processing parameters used in *LENS* are noted to affect the generation of porosity as well as phase evolution in the structure. Such variation in turn, modifies the mechanical properties of the alloys. While the porosity reduces significantly, existence of trace amount of precipitates along with an indication of co-existence of minute amount of martensite phase is apparent for the alloy manufactured with the highest laser energy density i.e. $NiTi_{\_E3}$. These microstructural modifications although have not influenced the hardness and elastic modulus of the alloy at the macro-scale, alter the values at lower load levels of micro- and nano-indentations. Additionally, the pseudoelastic recoverability of this functional material is also markedly influenced by the laser energy density. Consequently, $NiTi_{\_E3}$ alloy reveals higher hardness, reduced elastic modulus and pseudoelasticity. This is further confirmed on performing spherical nanoindentation on the alloys. A step forward is moved up on generating the indentation stress–strain curves, similar to that obtained from the conventional mechanical testing for the NiTi alloys. The graphs reflect not only the elastic and plastic, rather the pseudoelastic transformation and recovery distinctly especially at the small length scale. It is noted that the microstructures of *LENS* manufactured alloy changes along the different locations and planes which may affect the property variation as well. Hence, the localized mechanical properties of the alloys as evaluated by nanoindentation is complemented and validated with conventional bulk tensile testing along with the customized cyclic tensile tests. The later, complemented with the strain measurement using extensometer and *DIC* is particularly informative to assess the reversibility of *SIMT* mechanism in the *LENS* manufactured NiTi alloys leading to corresponding strain recoverability. From all the investigations, it is realized that best pseudoelastic recoverability along with a good combination of microstructural homogeneity, proper phase evolution and mechanical properties is obtained for the $NiTi_{\_E2}$ alloy. Such processing parameters therefore seem to be the optimum one.

Declaration of Competing Interest

The authors declare that they have no known competing financial interests or personal relationships that could have appeared to influence the work reported in this paper.

Acknowledgments

IS acknowledges the support of Alexander von Humboldt Foundation for the collaboration with Ruhr University, Bochum, Germany. The authors are also thankful to APM Technologies, India (GOM) for extending their support for some of the experiments reported. The financial support from Science and Engineering Research Board, Department of Science and Technology, India through research grant YSS/000976 is gratefully acknowledged. MD acknowledges the financial support from the Aeronautics Research & Development Board (AR&DB), India through project GAP0251.

Supplementary materials

Supplementary material associated with this article can be found, in the online version, at doi:10.1016/j.mtla.2019.100456.

References

[1] T. Duerig, A. Pelton, D. Stöckel, An overview of nitinol medical applications, Mater. Sci. Eng. A 273–275 (1999) 149–160, doi:10.1016/S0921-5093(99)00294-4.
[2] K. Otsuka, X. Ren, Physical metallurgy of Ti–Ni-based shape memory alloys, Prog. Mater. Sci. 50 (2005) 511–678, doi:10.1016/j.pmatsci.2004.10.001.
[3] M.L. Young, M.F. Wagner, J. Frenzel, W.W. Schmahl, G. Eggeler, Phase volume fractions and strain measurements in an ultrafine-grained NiTi shape-memory alloy during tensile loading, Acta Mater. 58 (2010) 2344–2354, doi:10.1016/j.actamat.2009.12.021.
[4] J.A. Shaw, S. Kyriakides, Thermomechanical aspects of NiTi, J. Mech. Phys. Solids 43 (1995) 1243–1281.
[5] C.P. Frick, T.W. Lang, K. Spark, K. Gall, Stress-induced martensitic transformations and shape memory at nanometer scales, Acta Mater. 54 (2006) 2223–2234, doi:10.1016/j.actamat.2006.01.030.
[6] D. Stoeckel, The shape memory effect – phenomenon, alloys, and applications, in: Proceedings of the Shape Memory Alloys for Power Systems, EPRI, 1995, pp. 1–13.
[7] J. Olbricht, M.F.X. Wagner, A. Condó, A. Dlouhy, C. Großmann, A. Kröger, C. Somsen, G. Eggeler, A transmission electron microscopy procedure for in-situ straining of miniature pseudoelastic NiTi specimens, Int. J. Mater. Res. 99 (2008) 1150–1156, doi:10.3139/146.101744.
[8] C. Haberland, H. Meier, J. Frenzel, On the properties of ni-rich NiTi shape memory parts produced by selective laser melting, in: Proceedings of the ASME 2012 conference on smart materials, adaptive structures and intelligent systems, SMASIS2012, 2012, pp. 1–8.
[9] M. Elahinia, N.S. Moghaddam, M.T. Andani, A. Amerinatanzi, B.A. Bimber, R.F. Hamilton, Fabrication of NiTi through additive manufacturing: a review, Prog. Mater. Sci. 83 (2016) 630–663, doi:10.1016/j.pmatsci.2016.08.001.
[10] C. Haberland, M. Elahinia, J.M. Walker, On the development of high quality NiTi shape memory and pseudoelastic parts by additive manufacturing, Smart Mater. Struct. 23 (2014) 1–13, doi:10.1088/0964-1726/23/10/104002.
[11] J.M. Walker, C. Haberland, M.T. Andani, E. Karaca, D. Dean, M. Elahinia, Process development and characterization of additively manufactured nickel–titanium shape memory parts, J. Intell. Mater. Syst. Struct. 27 (2016) 2653–2660, doi:10.1177/1045389X16635848.
[12] M.T. Andani, C. Haberland, J.M. Walker, M. Karamooz, A.S. Turabi, S. Saedi, R. Rahmanian, H. Karaca, D. Dean, M. Kadkhodaei, M. Elahinia, Achieving biocompatible stiffness in NiTi through additive manufacturing, J. Intell. Mater. Syst. Struct. 27 (2016) 2661–2671, doi:10.1177/1045389X16641199.
[13] J.J. Marattukalam, A. Kumar, S. Datta, M. Das, V. Krishna, S. Bontha, S.K. Kalpathy, Microstructure and corrosion behavior of laser processed NiTi alloy, Mater. Sci. Eng. C. 57 (2015) 309–313, doi:10.1016/j.msec.2015.07.067.
[14] S. Bernard, V.K. Balla, S. Bose, A. Bandyopadhyay, Rotating bending fatigue response of laser processed porous NiTi alloy, Mater. Sci. Eng. C 31 (2011) 815–820, doi:10.1016/j.msec.2010.12.007.
[15] S. Bernard, V.K. Balla, S. Bose, A. Bandyopadhyay, Compression fatigue behavior of laser processed porous NiTi alloy, J. Mech. Behav. Biomed. Mater. 13 (2012) 62–68, doi:10.1016/j.jmbbm.2012.04.010.
[16] B.V. Krishna, S. Bose, A. Bandyopadhyay, Fabrication of porous NiTi shape memory alloy structures using laser engineered net shaping, J. Biomed. Mater. Res. Part B Appl. Biomater. 89 (2009) 481–490, doi:10.1002/jbm.b.31238.
[17] C. Haberland, M. Elahinia, J. Walker, H. Meier, J. Frenzel, Additive manufacturing of shape memory devices and pseudoelastic components, in: Proceeding ASME 2013 Conference on Smart Materials, Adaptive Structures and Intelligent Systems SMASIS2013, 2013, pp. 1–8.
[18] H. Meier, C. Haberland, J. Frenzel, Structural and functional properties of NiTi shape memory alloys produced by selective laser melting, Adv. Res. Virtual Rapid Protyping. (2011) 291–296.
[19] F.A. España, V.K. Balla, S. Bose, A. Bandyopadhyay, Design and fabrication of CoCrMo alloy based novel structures for load bearing implants using laser engineered net shaping, Mater. Sci. Eng. C 30 (2010) 50–57, doi:10.1016/j.msec.2009.08.006.

[20] J. Frenzel, E.P. George, A. Dlouhy, C. Somsen, M.F.X. Wagner, G. Eggeler, Influence of Ni on martensitic phase transformations in NiTi shape memory alloys, Acta Mater. 58 (2010) 3444–3458, doi:10.1016/j.actamat.2010.02.019.

[21] J. Frenzel, J.A. Burow, E.J. Payton, S. Rezanka, G. Eggeler, Improvement of NiTi shape memory actuator performance through ultra-fine grained and nanocrystalline microstructures, Adv. Eng. Mater. 13 (2011) 256–268, doi:10.1002/adem.201000285.

[22] M. Rahim, J. Frenzel, M. Frotscher, J. Pfetzing-Micklich, R. Steegmüller, M. Wohlschlögel, H. Mughrabi, G. Eggeler, Impurity levels and fatigue lives of pseudoelastic NiTi shape memory alloys, Acta Mater. 61 (2013) 3667–3686, doi:10.1016/j.actamat.2013.02.054.

[23] B.V. Krishna, S. Bose, A. Bandyopadhyay, Laser processing of net-shape NiTi shape memory alloy, Metall. Mater. Trans. A 38 (2007) 1096–1103, doi:10.1007/s11661-007-9127-4.

[24] J.J. Marattukalam, V.K. Balla, M. Das, S. Bontha, S.K. Kalpathy, Effect of heat treatment on microstructure, corrosion, and shape memory characteristics of laser deposited NiTi alloy, J. Alloys Compd. 744 (2018) 337–346, doi:10.1016/j.jallcom.2018.01.174.

[25] J. Frenzel, A. Wieczorek, I. Opahle, B. Maaß, R. Drautz, G. Eggeler, On the effect of alloy composition on martensite start temperatures and latent heats in Ni–Ti-based shape memory alloys, Acta Mater. 90 (2015) 213–231, doi:10.1016/j.actamat.2015.02.029.

[26] A. Simchi, H. Pohl, Effects of laser sintering processing parameters on the microstructure and densification of iron powder, Mater. Sci. Eng. A 359 (2003) 119–128, doi:10.1016/S0921-5093(03)00341-1.

[27] ASTM Standard, F2004-17, Standard Test Method for Transformation Temperature of Nickel-Titanium Alloys by Thermal Analysis, ASTM International, 2004, pp. 1–5, doi:10.1520/F2004-17.2.

[28] I. Sen, U. Ramamurty, Elastic modulus of ti-6al-4v-xb alloys with B up to 0.55 wt%, Scr. Mater. 62 (2010) 37–40, doi:10.1016/j.scriptamat.2009.09.022.

[29] L. Marandi, I. Sen, Effect of saline atmosphere on the mechanical properties of commercial steel wire, Metall. Mater. Trans. A Phys. Metall. Mater. Sci. 50 (2019) 132–141, doi:10.1007/s11661-018-4956-x.

[30] ASTM E8/E8M-11, Standard test methods for tension testing of metallic materials, ASTM International ASTM Stds., 2013, pp. 1–28, doi:10.1520/E0008.

[31] Z. Dong, Y. Liu, W. Wen, J. Ge, J. Liang, Effect of hatch spacing on melt pool and as-built quality during selective laser melting of stainless steel: modeling and experimental approaches, Materials (Basel) 12 (2019) 1–15, doi:10.3390/ma12010050.

[32] B. Zheng, Y. Zhou, J.E. Smugeresky, J.M. Schoenung, E.J. Lavernia, Thermal behavior and microstructural evolution during laser deposition with laser-engineered net shaping: part I. numerical calculations, Metall. Mater. Trans. A 39A (2008) 2228–2236, doi:10.1007/s11661-008-9557-7.

[33] M. Xia, D. Gu, G. Yu, D. Dai, H. Chen, Influence of hatch spacing on heat and mass transfer, thermodynamics and laser processability during additive manufacturing of inconel 718 alloy, Int. J. Mach. Tools Manuf. 109 (2016) 147–157, doi:10.1016/j.ijmachtools.2016.07.010.

[34] E. Cakmak, P. Nandwana, D. Shin, Y. Yamamoto, M.N. Gussev, I. Sen, M.H. Seren, T.R. Watkins, J.A. Haynes, A comprehensive study on the fabrication and characterization of Ti–48Al–2Cr–2Nb preforms manufactured using electron beam melting, Materialia 6 (2019) 100284, doi:10.1016/j.mtla.2019.100284.

[35] D. Marini, D. Cunningham, J.R. Corney, Near net shape manufacturing of metal: a review of approaches and their evolutions, Proc. Inst. Mech. Eng. Part B J. Eng. Manuf. 232 (2018) 650–669, doi:10.1177/0954405417708220.

[36] F. Gao, H.M. Wang, Effect of TiNi in dry sliding wear of laser melt deposited Ti_2Ni/TiNi alloys, Mater. Charact. 59 (2008) 1349–1354, doi:10.1016/j.matchar.2008.05.007.

[37] G. Fei, W. Hua-Ming, Abrasive wear property of laser melting/deposited Ti2Ni/TiNi intermetallic alloy, Trans. Nonferrous Met. Soc. China 17 (2007) 1358–1362.

[38] R. Nagarajan, K. Chattopadhyay, Intermetallic Ti2Ni/TiNi nanocomposite by rapid solidification, Acta Metall. Mater. 42 (1994) 947–958.

[39] M. Arciniegas, J. Casals, J.M. Manero, J. Peña, F.J. Gil, Study of hardness and wear behaviour of NiTi shape memory alloys, J. Alloys Compd. 460 (2008) 213–219, doi:10.1016/j.jallcom.2007.05.069.

[40] L. Bataillard, J.-.E. Bidaux, R. Gotthardt, Interaction between microstructure and multiple-step transformation in binary NiTi alloys using *in-situ* transmission electron microscopy observations, Philos. Mag. A 78 (1998) 327–344, doi:10.1080/01418619808241907.

[41] J. Uchil, K.P. Mohanchandra, K.K. Mahesh, K. Ganesh Kumara, Thermal and electrical characterization of R-phase dependence on heat-treat temperature in Nitinol, Phys. B 253 (1998) 83–89, doi:10.1016/S0921-4526(98)00378-0.

[42] X. Zhang, H. Sehitoglu, Crystallography of the B2 → r → B19′ phase transformations in NiTi, Mater. Sci. Eng. A 374 (2004) 292–302, doi:10.1016/j.msea.2004.03.013.

[43] P. Šittner, M. Landa, P. Lukáš, V. Novák, R-phase transformation phenomena in thermomechanically loaded NiTi polycrystals, Mech. Mater. 38 (2006) 475–492, doi:10.1016/j.mechmat.2005.05.025.

[44] K. Gall, H. Sehitoglu, Y.I. Chumlyakov, I.V. Kireeva, Tension-Compression asymmetry of the stress–strain response in the aged single crystal and polycrystalline NiTi, Acta Mater. 47 (1999) 1203–1217.

[45] A.C. Fischer-Cripps, Nanoindentation, Springer, Mech. Eng. Ser. (2002).

[46] Q. Kan, W. Yan, G. Kang, Q. Sun, Oliver-Pharr indentation method in determining elastic moduli of shape memory alloys – a phase transformable material, J. Mech. Phys. Solids 61 (2013) 2015–2033, doi:10.1016/j.jmps.2013.05.007.

[47] https://www.hysitron.com/media/1683/t-003-v30-probe-calibration.pdf, August 14, 2017, (n.d.).

[48] I. Sen, H. Jirková, B. Mašek, M. Böhme, M.F.-X. Wagner, Microstructure and mechanical behavior of a mini-thixoformed tool steel, Metall. Mater. Trans. A. 43 (2012) 3034–3038, doi:10.1007/s11661-012-1305-3.

[49] I. Sen, S. Roy, M.F.X. Wagner, Indentation response and structure-property correlation in a bimodal Ti–6Al–4V Alloy, Adv. Eng. Mater. 19 (2017) 1–12, doi:10.1002/adem.201700298.

[50] P. Sittner, L. Heller, J. Pilch, C. Curfs, T. Alonso, D. Favier, Young's modulus of austenite and martensite phases in superelastic NiTi wires, J. Mater. Eng. Perform. 23 (2014) 2303–2314, doi:10.1007/s11665-014-0976-x.

[51] S.-.Y. Jiang, Y.-.N. Zhao, Y. Zhang, L. Hu, Y. Liang, Effect of solution treatment and aging on microstructural evolution and mechanical behavior of NiTi shape memory alloy, Trans. Nonferrous Met. Soc. China 23 (2013) 3658–3667, doi:10.1016/S1003-6326(13)62914-3.

[52] M. Prayab, N. Asghar, O. Bayat, V. Abouei, A. Eshraghi, Effect of heat treatment on the microstructural and superelastic behavior of NiTi alloy with 58.5wt% Ni, Assoc, Metall. Eng. Serbia. 16 (2010) 123–131.

[53] Y. Fu, W. Huang, H. Du, X. Huang, J. Tan, X. Gao, Characterization of TiNi shape-memory alloy thin films for MEMS applications, Surf. Coatings Technol. 145 (2001) 107–112, doi:10.1016/S0257-8972(01)01324-X.

[54] F. Gao, H.M. Wang, Dry sliding wear property of a laser melting / deposited Ti2Ni/TiNi intermetallic alloy, Intermetallics 16 (2008) 202–208, doi:10.1016/j.intermet.2007.09.008.

[55] S. Moyne, C. Poilane, K. Kitamura, S. Miyazaki, P. Delobelle, C. Lexcellent, Analysis of the thermomechanical behavior of Ti–Ni shape memory alloy thin films by bulging and nanoindentation procedures, Mater. Sci. Eng. A 273–275 (1999) 727–732, doi:10.1016/S0921-5093.

[56] A. Amini, C. Cheng, Nature of hardness evolution in nanocrystalline NiTi shape memory alloys during solid-state phase transition, Sci. Rep. 3 (2013) 1–7, doi:10.1038/srep02476.

[57] A. Amini, W. Yan, Q. Sun, Depth dependency of indentation hardness during solid-state phase transition of shape memory alloys, Appl. Phys. Lett. 99 (2011) 1–3, doi:10.1063/1.3603933.

[58] W.D. Nix, H.J. Gao, Indentation size effects in crystalline materials: a law for strain gradient plasticity, J. Mech. Phys. Solids 46 (1998) 411–425, doi:10.1016/s0022-5096(97)00086-0.

[59] Y. Huang, F. Zhang, K.C. Hwang, W.D. Nix, G.M. Pharr, G. Feng, A model of size effects in nano-indentation, J. Mech. Phys. Solids. 54 (2006) 1668–1686, doi:10.1016/j.jmps.2006.02.002.

[60] Y.V. Milman, A.A. Golubenko, S.N. Dub, Indentation size effect in nanohardness, Acta Mater. 59 (2011) 7480–7487, doi:10.1016/j.actamat.2011.08.027.

[61] Z. Peng, J. Gong, H. Miao, On the description of indentation size effect in hardness testing for ceramics: analysis of the nanoindentation data, J. Eur. Ceram. Soc. 24 (2004) 2193–2201, doi:10.1016/S0955-2219(03)00641-1.

[62] G.Z. Voyiadjis, R. Peters, Size effects in nanoindentation: an experimental and analytical study, Acta Mech. 211 (2010) 131–153, doi:10.1007/s00707-009-0222-z.

[63] G.B. Viswanathan, E. Lee, D.M. Maher, S. Banerjee, H.L. Fraser, Direct observations and analyses of dislocation substructures in the α phase of an α/β Ti-alloy formed by nanoindentation, Acta Mater. 53 (2005) 5101–5115, doi:10.1016/j.actamat.2005.07.030.

[64] N.A. Fleck, J.W. Hutchinson, A phenomenological theory for strain gradient effects in plasticity, J. Mech. Phys. Solids 41 (1993) 1825–1857, doi:10.1016/0022-5096(93)90072-N.

[65] R.A. Mirshams, R.M. Pothapragada, Correlation of nanoindentation measurements of nickel made using geometrically different indenter tips, Acta Mater. 54 (2006) 1123–1134, doi:10.1016/j.actamat.2005.10.048.

[66] G. Farges, D. Degout, Interpretation of the indentation size effect in vickers microhardness measurements-absolute hardness of materials, Thin Solid Films 181 (1989) 365–374, doi:10.1016/0040-6090(89)90505-1.

[67] C. Maletta, F. Furgiuele, E. Sgambitterra, M. Callisti, B.G. Mellor, R.J.K. Wood, Indentation response of a NiTi shape memory alloy : modeling and experiments, Frat. Ed Integrita Strutt. 21 (2012) 5–12, doi:10.3221/IGF-ESIS.21.01.

[68] J. Pfetzing, M.F.-X. Wagner, T. Simon, A. Schaefer, C. Somsen, G. Eggeler, TEM investigation of the microstructural evolution during nanoindentation of NiTi, in: Proceedings of the ESOMAT 2009, 06027, 2009, pp. 1–7, doi:10.1051/esomat/200906027.

[69] J. Pfetzing-Micklich, M.F.-X. Wagner, R. Zarnetta, J. Frenzel, G. Eggeler, A.E. Markaki, J. Wheeler, T.W. Clyne, Nanoindentation of a pseudoelastic NiTife shape memory alloy, Adv. Eng. Mater. 12 (2010) 13–19, doi:10.1002/adem.200900266.

[70] A.J. Muir Wood, T.W. Clyne, Measurement and modelling of the nanoindentation response of shape memory alloys, Acta Mater. 54 (2006) 5607–5615, doi:10.1016/j.actamat.2006.08.013.

[71] Z.Y. Yang, X.H. Zheng, W. Cai, Martensitic transformation and shape memory effect of Ti–V–Al lightweight high-temperature shape memory alloys, Scr. Mater. 99 (2015) 97–100, doi:10.1016/j.scriptamat.2014.11.038.

[72] A.J. Muir Wood, S. Sanjabi, Y.Q. Fu, Z.H. Barber, T.W. Clyne, Nanoindentation of binary and ternary Ni–Ti-based shape memory alloy thin films, Surf. Coatings Technol. 202 (2008) 3115–3120, doi:10.1016/j.surfcoat.2007.11.011.

[73] Y.-.T. Cheng, D.S. Grummon, Indentation in shape memory alloys, in: Y. Fuqian, J.C.M. Li (Eds.), Micro and Nano Mechanical Testing of Materials and Devices, Springer Science+Business Media, LLC, New York, 2008, pp. 71–86.

[74] C.P. Frick, A.M. Ortega, J. Tyber, A.E.M. Maksound, H.J. Maier, Y. Liu, K. Gall, Thermal processing of polycrystalline NiTi shape memory alloys, Mater. Sci. Eng. A 405 (2005) 34–49, doi:10.1016/j.msea.2005.05.102.

[75] S. Pathak, S.R. Kalidindi, Spherical nanoindentation stress –strain curves, Mater. Sci. Eng. R 91 (2015) 1–36, doi:10.1016/j.mser.2015.02.001.

[76] Y. Liu, H. Xiang, Apparent modulus of elasticity of near-equiatomic NiTi, J. Alloys Compd. 270 (1998) 154–159.
[77] K.N. Melton, O. Mercier, The mechanical properties of NiTi-based shape memory alloys, Acta Metall. 29 (1981) 393–398, doi:10.1016/0001-6160(81)90165-6.
[78] H. Sehitoglu, I. Karaman, R. Anderson, X. Zhang, K. Gall, H.J. Maier, Y. Chumlyakov, Compressive response of NiTi single crystals, Acta Mater. 48 (2000) 3311–3326, doi:10.1016/S1359-6454(00)00153-1.
[79] D.M. Norfleet, P.M. Sarosi, S. Manchiraju, M.F. Wagner, M.D. Uchic, P.M. Anderson, M.J. Mills, Transformation-induced plasticity during pseudoelastic deformation in Ni– Ti microcrystals, Acta Mater. 57 (2009) 3549–3561, doi:10.1016/j.actamat.2009.04.009.
[80] A. Yawny, J. Olbricht, M. Sade, G. Eggeler, Pseudoelastic cycling and aging effects at ambient temperature in nanocrystalline Ni-rich NiTi wire, Mater. Sci. Eng. A 481–482 (2008) 86–90, doi:10.1016/j.msea.2007.04.124.
[81] J. Ferčec, I. Anžel, R. Rudolf, Stress dependent electrical resistivity of orthodontic wire from the shape memory alloy NiTi, Mater. Des. 55 (2014) 699–706, doi:10.1016/j.matdes.2013.10.041.
[82] Y. Xiao, P. Zeng, L. Lei, Y. Zhang, In situ observation on temperature dependence of martensitic transformation and plastic deformation in superelastic NiTi shape memory alloy, Mater. Des. 134 (2017) 111–120, doi:10.1016/j.matdes.2017.08.037.
[83] C. Elibol, M.F.X. Wagner, Investigation of the stress-induced martensitic transformation in pseudoelastic NiTi under uniaxial tension, compression and compression-shear, Mater. Sci. Eng. A 621 (2015) 76–81, doi:10.1016/j.msea.2014.10.054.
[84] N. Zotov, M. Pfund, E. Polatidis, A.F. Mark, E.J. Mittemeijer, Change of transformation mechanism during pseudoelastic cycling of NiTi shape memory alloys, Mater. Sci. Eng. A 682 (2017) 178–191, doi:10.1016/j.msea.2016.11.052.
[85] A. Schaefer, M.F.-X. Wagner, Strain mapping at propagating interfaces in pseudoelastic NiTi, ESOMET 06031 (2009) 1–6, doi:10.1051/esomat/200906031.